frontiers | Frontiers in Soft Matter

TYPE Original Research
PUBLISHED 21 May 2024
DOI 10.3389/frsfm.2024.1359128

OPEN ACCESS

EDITED BY
Frank Alexis,
Universidad San Francisco de Quito, Ecuador

REVIEWED BY
Anne-laure Fameau,
Institut National de recherche pour l'agriculture, l'alimentation et l'environnement (INRAE), France
Konstantin Kornev,
Clemson University, United States

*CORRESPONDENCE
Alejandro D. Rey,
alejandro.rey@mcgill.ca

RECEIVED 20 December 2023
ACCEPTED 16 April 2024
PUBLISHED 21 May 2024

CITATION
Zamora Cisneros DU, Wang Z, Dorval Courchesne N-M, Harrington MJ and Rey AD (2024), Geometric modeling of phase ordering for the isotropic–smectic A phase transition.
Front. Soft Matter 4:1359128.
doi: 10.3389/frsfm.2024.1359128

Geometric modeling of phase ordering for the isotropic–smectic A phase transition

David Uriel Zamora Cisneros[1], Ziheng Wang[1], Noémie-Manuelle Dorval Courchesne[1], Matthew J. Harrington[2] and Alejandro D. Rey[1]*

[1]Department of Chemical Engineering, McGill University, Montreal, QC, Canada, [2]Department of Chemistry, McGill University, Montreal, QC, Canada

Background: Liquid crystal (LC) mesophases have an orientational and positional order that can be found in both synthetic and biological materials. These orders are maintained until some parameter, mainly the temperature or concentration, is changed, inducing a phase transition. Among these transitions, a special sequence of mesophases has been observed, in which priority is given to the direct smectic liquid crystal transition. The description of these transitions is carried out using the Landau–de Gennes (LdG) model, which correlates the free energy of the system with the orientational and positional order.

Methodology: This work explored the direct isotropic-to-smectic A transition studying the free energy landscape constructed with the LdG model and its relation to three curve families: (I) level-set curves, steepest descent, and critical points; (II) lines of curvature (LOC) and geodesics, which are directly connected to the principal curvatures; and (III) the Casorati curvature and shape coefficient that describe the local surface geometries resemblance (sphere, cylinder, and saddle).

Results: The experimental data on 12-cyanobiphenyl were used to study the three curve families. The presence of unstable nematic and metastable plastic crystal information was found to add information to the already developed smectic A phase diagram. The lines of curvature and geodesics were calculated and laid out on the energy landscape, which highlighted the energetic pathways connecting critical points. The Casorati curvature and shape coefficient were computed, and in addition to the previous family, they framed a geometric region that describes the phase transition zone.

Conclusion and significance: A direct link between the energy landscape's topological geometry, phase transitions, and relevant critical points was established. The shape coefficient delineates a stability zone in which the phase transition develops. The methodology significantly reduces the impact of unknown parametric data. Symmetry breaking with two order parameters (OPs) may lead to novel phase transformation kinetics and droplets with partially ordered surface structures.

KEYWORDS

liquid crystals, smectic A, phase transition, energy landscape, shape coefficient, free energy, Landau–de Gennes

1 Introduction

Synthetic and biological liquid crystals (LCs) are anisotropic soft materials with partial degrees of orientational and positional order, conveying fluidity as viscous liquids and anisotropy as in the crystalline order (Rey and Denn, 2002; Donald et al., 2006; Rey, 2010; Sonnet and Virga, 2012; Petrov, 2013; Lagerwall, 2016; Selinger, 2016; Collings and Goodby, 2019; Stewart, 2019; Zannoni, 2022). Importantly, possible LC mesogens include rod-, board-, disk-, and screw-like molecules with flexibilities ranging from semi-flexible to rigid, involving monomers or main/side-chain polymers and colloids (Donald et al., 2006; Demus et al., 2008b; Demus et al., 2011). The synthesis and formation of these mesophase materials follow equilibrium self-assembly processes driven by temperature (thermotropic), concentration (lyotropic), or both (Bowick et al., 2017; Wang et al., 2023b). The presence of multiple components, as in nanoparticle-loaded mesophases, gives rise to couplings between self-assembly and phase separation with states that can combine the crystallinity (positional order) of one component with the liquid crystallinity (various degrees of positional and orientational order) of the other (Soulé et al., 2012a; Soulé et al., 2012b; Soulé et al., 2012c; Soule and Rey, 2012; Milette et al., 2013; Gurevich et al., 2014). Various external fields (flow, electromagnetic, and thermal) can be used to generate self-organized structures not seen in purely equilibrium self-assembly. The natural setting to describe self-assembly starts with the energy landscape and its geometrical properties (curvatures, cusps, domes, *etc.*), while for non-equilibrium organization, the natural setting will include the entropy production landscape and its defining geometric measures. In this paper, we present a widely applicable geometry-based methodology for describing self-assembly in anisotropic soft matter and target one specific transition that exhibits complex ordering processes. Without ambiguity, for convenience and brevity, below we refer to self-assembly as phase ordering and/or phase transition, as we do not include phase separation and conserved quantities. In addition, we refer to the degree of quench as the equivalent of the thermodynamic driving force for phase ordering.

The spectrum of self-assembly processes is significantly enriched when considering the sequence of phase transformations. This progression follows an increase in order as the magnitude of the thermodynamic driving force is increased, corresponding to a decrease in temperature for thermotropes or an increase in concentration for lyotropes. The sequence then goes from a high-symmetry isotropic state to an orientationally ordered (nematic) state. This state is then followed by the addition of the positional order (smectic). Then, the crystalline organization is reached with a further increase in the driving force. The usual sequence of isotropic–orientational–positional phase ordering (Oswald and Pieranski, 2005a; Jákli and Saupe, 2006; Blinov, 2011) is sometimes reordered to a direct isotropic–positional/orientational ordering, as observed in monomeric thermotropes (certain cyano-biphenyls (CB) and oxy-cyanobiphenyls (OCB)) (Oh, 1977; Idziak et al., 1996; Oswald and Pieranski, 2005b; Donald et al., 2006; Abukhdeir and Rey, 2008; Chahine et al., 2010; Gudimalla et al., 2021; Nesrullajev, 2022) and biological liquid crystals (BLCs) such as collagen mesophase precursors in the mussel byssus (Knight and Vollrath, 1999; Viney, 2004; Donald et al., 2006; Rey, 2010; Rey and Herrera-Valencia, 2012; Rey et al., 2013; Renner-Rao et al., 2019; Manolakis and Azhar, 2020; Harrington and Fratzl, 2021; Berent et al., 2022). This important and non-classical behavior is the focus of this paper: the direct isotropic-to-smectic A (I-SmA) LC phase transition, where SmA denotes the simplest smectic phase. A collection of compounds exhibiting this scheme can be found (Hawkins and April 1983; Idziak et al., 1996; Lenoble et al., 2007; Abukhdeir and Rey, 2008; Mohieddin Abukhdeir and Rey, 2008a; Li et al., 2009; Wojcik et al., 2009; Chahine et al., 2010; Pouget et al., 2011; Salamonczyk et al., 2016; Bradley, 2019; Renner-Rao et al., 2019; Gudimalla et al., 2021; Jackson et al., 2021; Jehle et al., 2021; Khadem and Rey, 2021; Nesrullajev, 2022), which is largely driven by attractive forces in thermotropic LCs [e.g., cyanobiphenyl family (n-CB, n > 10) (Bellini et al., 2002)] and excluded volume interactions in BLCs (e.g., collagen in mussel byssus and Ff phages). In both cases, a common geometric feature is the presence of rigid or semi-rigid rod-like cores and sufficiently long semi-flexible ends. Currently, the best-characterized materials that follow the direct I-SmA are low-molar mass thermotropic LCs, such as 10CB and 12CB (Collings, 1997; Urban et al., 2005; Demus et al., 2008a; Li et al., 2009; Chahine et al., 2010; Gudimalla et al., 2021; Zaluzhnyy et al., 2022). To avoid introducing a plethora of unknown parameters and material data, we focus on them as model systems. In the future, our ultimate goal is to expand the findings to lyotropic polymeric and colloidal smectics that are found in collagen precursors of the mussel byssus (Renner-Rao et al., 2019; Jehle et al., 2021; Waite and Harrington, 2022). It is noted that even though we only consider thermotropic LCs in the current manuscript, using correspondence principles such as those provided in the following references (Picken, 1990; Soule and Rey, 2011; Golmohammadi and Rey, 2009; Doi, 1981), we can, in the future, use the current findings for collagen-based LCs.

A key feature of the I-SmA transition is the strong coupling of the positional and orientational order parameters (OPs) (Pikin, 1991; Gorkunov et al., 2007; Blinov, 2011; Turek et al., 2020; Gurin et al., 2021), which results in the enhancement of the orientational OP over and above what a nematic phase could show at these conditions of temperature or concentration. A practical consequence of this, as we know from synthetic liquid crystal polymers (LCPs), is that in the solid state, the enhanced orientational order parameter has a strong impact on the mechanical properties (e.g., Young modulus) that can be seen in LCP fibers (Ward, 1993; Ziabicki, 1993; Donald et al., 2006; Turek et al., 2020; Bunsell et al., 2021). This order parameter coupling decreases the free energy of the system to result in a smectic A phase at minimal quenches from the stable disordered state. Polymeric and biological liquid-crystalline materials, being part of the lyo/thermotropic spectrum, also share the preferred native mode of fiber-formation, as seen in their *in vivo* and *in vitro* states (Matthews et al., 2002; Viney, 2004; Dierking and Al-Zangana, 2017; Renner-Rao et al., 2019; Deng et al., 2021; Harrington and Fratzl, 2021; Tortora and Jost, 2021; Cai et al., 2023; Zhang et al., 2023), which reinforces the hypothesis of smecticity enhancing the material's mechanical properties through increased alignment.

The computational liquid crystal phase-field methodology used in this paper, largely based on the Landau–de Gennes (LdG) models and their many generalizations, has been widely used to simulate and predict self-assembly, self-organization, rheology, bulk,

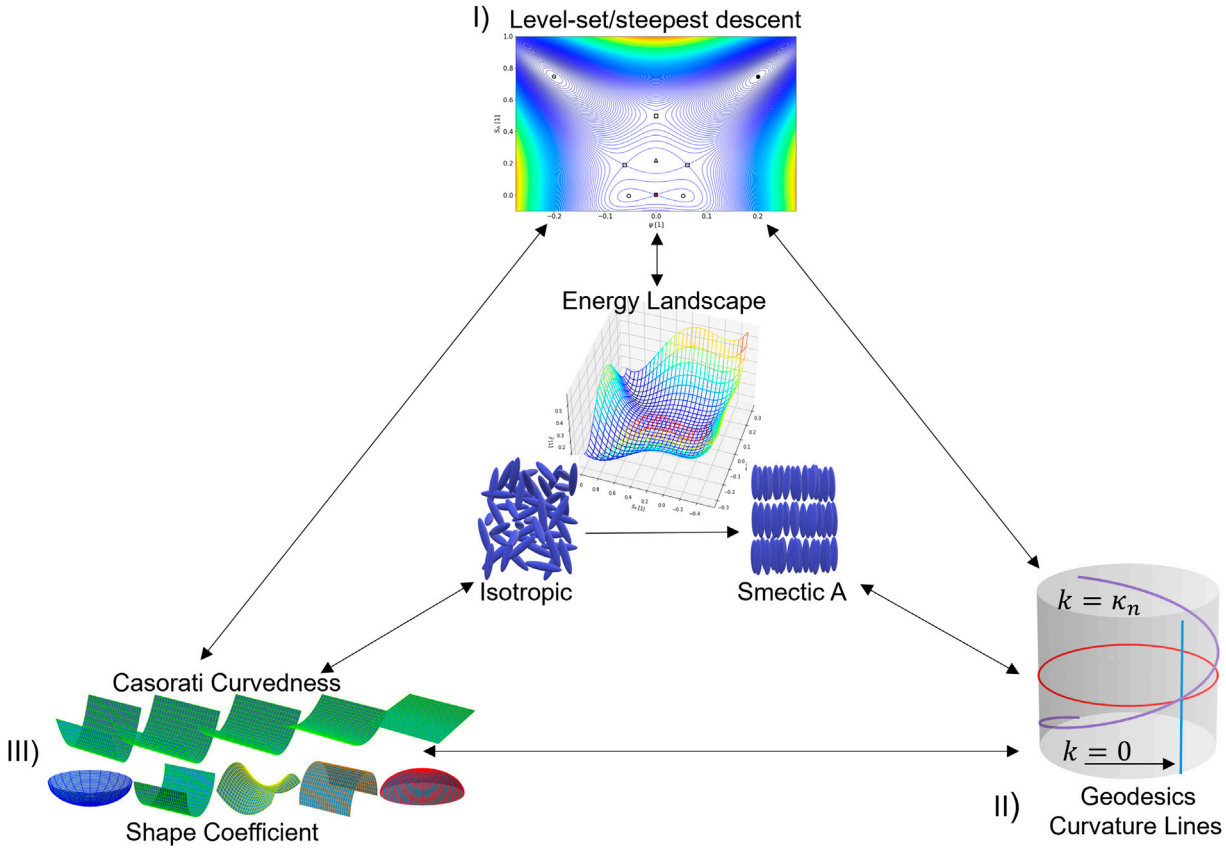

FIGURE 1
Methodology of the geometric-thermodynamics formulated (Section 2) and implemented (Section 3) in this paper. The central energy landscape corresponding to the direct I-SmA transition is characterized using three geometric methods (I) level sets/steepest descent/critical points, (II) geodesics and curvature lines, and (III) shape and Casorati curvedness analysis; the bottom left shows changes in shape from cup (left), to rut, saddle, ridge, and cap (right) and changes in the degree of curvedness for a rut patch (left) into a flat plane. The outer arrows show the connection and integration of the three calculations.

interfacial transport phenomena, and more for both thermotropic and lyotropic LCs (Biscari et al., 2007; Hormann and Zimmer, 2007; Popa-Nita and Sluckin, 2007; Saunders et al., 2007; Mohieddin Abukhdeir and Rey, 2008b; Rey, 2010; Coles and Strazielle, 2011; Garti et al., 2012; Mukherjee, 2014; Han et al., 2015; Selinger, 2016; Collings and Hird, 2017; Vitral et al., 2019; Copic and Mertelj, 2020; Vitral et al., 2020; Schimming et al., 2021; Bukharina et al., 2022; Paget et al., 2022; Zaluzhnyy et al., 2022). As in other coupled OP transitions, the challenges for a given energy landscape include the following issues:

- What is the total number of local maxima, minima, and saddles in the energy surface for a given quench?
- Where are the local minima and maxima located for a given quench?
- When do we find bi-stability?
- What states exist when one of the OPs is zero (e.g., nematic and plastic crystal)?
- What are the shortest path directions connecting minima?

Previous works have excellently characterized these mesophases and phase transitions, including phase diagrams, orientation distribution function profiles, bifurcation analysis, and the use of imaging techniques, calorimetry characterization, and dynamic simulations, accentuating the thermodynamic I-SmA phase transition perspective (Palffy-Muhoray, 1999; Dogic and Fraden, 2001; Mukherjee et al., 2001; Larin, 2004; Urban et al., 2005; Biscari et al., 2007; Das and Mukherjee, 2009; Chahine et al., 2010; Nandi et al., 2012; Izzo and De Oliveira, 2019; Gudimalla et al., 2021; Khan and Mukherjee, 2021; Mukherjee, 2021). Given that the first four key issues are essentially anchored in the spatial features of the energy landscape, we develop, implement, and validate a novel geometric methodology. The use of geometric methods to characterize thermodynamics, phase transitions, and energy landscapes has been widely recognized as a useful and complementary set of tools (Miller, 1925; Hormann and Zimmer, 2007; Quevedo et al., 2011; Wales, 2018; Wang et al., 2020; Demirci and Holland, 2022; Liu et al., 2022; Quevedo et al., 2022). These approaches rely on establishing a proper thermodynamic surface in terms of variables such as pressure, temperature, and chemical potential. Here, we extend and generalize these geometric-thermodynamic methods for self-assembly in anisotropic soft matter in general and phase ordering in the I-SmA transition. The methodology is summarized in Figure 1. The triangle's center is the key focus of this paper, the direct isotropic-SmA transition, as characterized by an energy landscape given by the Landau free energy $F(\psi, S_A)$ as a

function of the positional (ψ) and orientational (S_A) order parameters for a given temperature T. Importantly, the surface parametrization is explicit and known as Monge parameterization, and it is the starting point for the geometric methodology developed in this paper.

In (I), at the upper vertex from Figure 1, the critical points (dots) of the surface (maxima, minima, and saddles) are determined as a function of changes in temperature using level-set curves and curves of the steepest descent. The closed loops in the former allow the detection of minima/maxima and saddles, and the signs of the gradient curves differentiate the stable from the unstable. In addition, saddles in the level sets are unstable points. These calculations are guided and validated using the powerful index theorem of polynomials, yielding a conservation equation for the number of maxima N_{maxima}, the number of minima N_{minima}, and the number of saddles N_{saddles}. At a high temperature for a stable isotropic phase, the landscape is simple and $N_{\text{maxima}} = N_{\text{saddles}} = 0$, but for low quenches with a stable SmA phase, the landscape is complex, as we find $N_{\text{minima}} = N_{\text{saddles}} = 4$ and $N_{\text{maxima}} = 1$. In (II), at the lower right vertex, the geodesic lines of the energy landscape are found using accurate ordinary differential equation (ODE) solvers. Importantly, the lack of torsion in the geodesic lines correlates with the energy heights of the maxima and minima. In (II), we also compute the lines of curvature (LOC) that define an orthogonal grid on the energy surface and indicate the maximum or minimum directional curvature flow. In (III), the shape coefficient, or shape index S, relates a given value with a shape that comes from the spectrum $S = \pm 1$ for up/down half-spheres (cup and cap, respectively), $S = \pm 1/2$ for up/down cylinders (rut and ridge, respectively), and $S = 0$ for saddle-like shapes; the positive scalar curvedness Casorati curvature C (surface deviation from planarity) of the energy landscape and its critical points are identified to determine aspects of the minima and maxima, such as anisotropy, the presence or absence of umbilic $S = \pm 1$ points, and the degree of curvedness (magnitude of Casorati curvature), and detect maxima/minima/saddles in a fast and efficient way.

Describing the shape using the dimensionless normalized shape coefficient (S) avoids co-mingling properties associated with shape with those associated with curvedness, such as when using the classical differential geometry descriptions based on Gaussian (K), mean (H), and deviatoric (D) curvatures. The shape coefficient–Casorati curvedness (S, C) method has been successfully applied to several soft-matter materials and equilibrium and dissipative processes (Wang et al., 2020; Wang et al., 2022b; Wang et al., 2022a; Wang et al., 2023b). For example, for a saddle point, the classical approach yields $K = -D^2$. On the other hand, the (S, C) method detects a saddle simply when $S = 0$ and its curvedness is $C = D = \sqrt{-K}$. Finally, the arrows on the triangle side and toward the center denote the integration of the methods to shed new light on the I-SmA transition.

This work builds on the fundamental studies on the self-assembled smectic phase transition (Pleiner et al., 2000; Mukherjee et al., 2001; Abukhdeir, 2009; Abukhdeir and Rey, 2009b; Mukherjee, 2021). The particular objectives of this paper are the following:

- Characterize the energy landscape using a simple Monge parametrization in terms of nematic and smectic order parameters, including the number and type of critical points and characteristic trajectories between stable, metastable, and unstable isotropic, nematic, and smectic states as a function of the changing degrees of quenching from the isotropic state.
- Use classical curvatures (Gaussian and mean) and new soft matter geometric methods (shape coefficient and Casorati curvedness) to shed light on where saddles and cusps are located and their curvedness, thus providing a broad picture of the energy landscape.
- Integrate thermodynamic stability, polynomial-based charge conservation methods, and geometric methods.
- Detect and characterize unstable nematic and metastable plastic crystal states that emerge at medium and large degrees of quenching.

The remainder of this paper is organized as follows: Section 2 presents the OPs, Landau free energy (Section 2.1), geometric thermodynamics (Section 2.2), and computational methods (Section 2.3). Section 3 presents the results and discussion. Section 4 summarizes the key findings, their significance, and the novelty of the geometric approach.

2 Methodology

2.1 Order parameters and Landau model

2.1.1 Nematic and smectic A phases: orientational and positional order parameters

The SmA LC phase has partial 1D positional and orientational order. Two order parameters, the orientational order parameter $\mathbf{Q}$ and the positional order parameter $\mathbf{\Psi}$, are used for this mesophase characterization. These parameters capture the average molecular order by the establishment of distinctive moduli at the transition, with the moduli (S_A, P) for the orientation and ψ for the position (Oswald and Pieranski, 2005b; Rey, 2010; Mukherjee, 2014; Vitral et al., 2020).

The theoretical characterization of the partial orientational alignment in LCs is described by an orientation distribution function, the tensor order parameter $\mathbf{Q}$ (De Gennes and Prost, 1993), which is as follows:

$$\mathbf{Q} = S_A\left(\mathbf{nn} - \frac{\mathbf{I}}{3}\right) + \frac{1}{3}P(\mathbf{mm} - \mathbf{ll}), \tag{2.1}$$

where $\mathbf{n}$, $\mathbf{m}$, and $\mathbf{l}$ are the molecular unit vectors and $\mathbf{I}$ is the unit tensor. The $\mathbf{Q}$ tensor is expressed in terms of the orthonormal director triad ($\mathbf{n}$, $\mathbf{m}$, and $\mathbf{l}$), which are the eigenvectors of $\mathbf{Q}$ that describe the molecular axes and the scalar moduli (S_A, P) that measure the magnitude of the average molecular orientation (De Luca and Rey, 2006; Coles and Strazielle, 2011). The $\mathbf{Q}$ tensor is symmetric and traceless, i.e., $\mathbf{Q} = \mathbf{Q}^T$ and $\mathbf{Q}$: $\mathbf{I} = 0$, and it has five independent components. It is comprised of uniaxial (S_A and $\mathbf{n}$) and biaxial (P and $\mathbf{m}, \mathbf{l}$) contributions. The uniaxial contribution $S_A = \frac{3}{2}(\mathbf{nn}: \mathbf{Q})$ corresponds to the major eigenvalue/eigenvector, and the biaxial contribution $P = \frac{3}{2}(\mathbf{mm} - \mathbf{ll})$: $\mathbf{Q}$ corresponds to the minor eigenvalues/eigenvectors. A free-energy expansion near the nematic transition, as per the Landau formalism, was defined, yielding an LdG free-energy expression for nematic orientational alignment F_N

(de Gennes and Prost, 1993), truncated up to the fourth-order term with respect to S_A as follows:

$$F_N = F_0 + \frac{1}{2}a(\mathbf{Q}\colon \mathbf{Q}) - \frac{1}{3}b(\mathbf{Q}\cdot\mathbf{Q})\colon \mathbf{Q} + \frac{1}{4}c(\mathbf{Q}\colon \mathbf{Q})^2 + \ldots, \quad (2.2)$$

where F_0 is the energy of the isotropic state, $a = a_0(T - T^*_{NI})$, T^*_{NI} is the critical nematic phase transition temperature, and a_0, b, and c are experimentally measured material parameters.

In addition to the orientational organization, due to its lamellar configuration and the periodic structure of the uniaxial SmA phase, a one-dimensional positional order parameter is required, and the complex wave vector $\boldsymbol{\Psi}$ has been widely used for this purpose (Mukherjee et al., 2001; Abukhdeir and Rey, 2009c; Vitral et al., 2020). It is typified by the phase ϕ, and its modulus ψ characterizes a one-dimensional density wave used to describe such a layered nature as follows:

$$\boldsymbol{\psi} = \psi e^{i\phi}. \quad (2.3)$$

Then, a free-energy functional of the smectic positional order, F_S, is introduced, accounting for positional ordering, and the material-dependent parameters are $\alpha = \alpha_0(T - T^*_{AI})$ and β around the critical smectic transition temperature T^*_{AI}.

$$F_S = \alpha|\boldsymbol{\psi}|^2 + \beta|\boldsymbol{\psi}|^4 + \cdots. \quad (2.4)$$

In the simplest case, the I-SmA transition is captured by the free-energy contributions of the form $F = F_N + F_S + F_{NS}$, where F_{NS} is the coupling free-energy term, which is given as follows:

$$F_{NS} = -\delta|\boldsymbol{\psi}|(\mathbf{Q}\colon \mathbf{Q}) - \frac{1}{2}e\mathbf{Q}\colon (\nabla\boldsymbol{\psi}\nabla\boldsymbol{\psi}) + \frac{1}{2}b_1|\nabla\boldsymbol{\psi}|^2 + \frac{1}{4}b_2|\nabla^2\boldsymbol{\psi}|^2. \quad (2.5)$$

2.1.2 Landau model for the isotropic–smectic A transition

The well-established models have been formulated and used to describe the I-SmA transition, including non-direct transitions (Pleiner et al., 2000; Abukhdeir and Rey, 2009b; Nandi et al., 2012; Pevnyi et al., 2014; Izzo and De Oliveira, 2019; Mukherjee, 2021; Paget et al., 2022). These models include the nematic and smectic contributions (Eqs. 2.2, 2.4, and 2.5) and consolidate the final total free-energy density using coupling terms (δ, e) that favor one phase over the other and terms that account for the energy cost from the coexistence of the positional ordering (b_1, b_2):

$$\text{Total Energy} = \int F\,dV$$

$$F = F_0 + \frac{1}{2}a(\mathbf{Q}\colon \mathbf{Q}) - \frac{1}{3}b(\mathbf{Q}\cdot\mathbf{Q})\colon \mathbf{Q} + \frac{1}{4}c(\mathbf{Q}\colon \mathbf{Q})^2 + \alpha|\boldsymbol{\psi}|^2 + \beta|\boldsymbol{\psi}|^4 - \delta|\boldsymbol{\psi}|(\mathbf{Q}\colon \mathbf{Q}) - \frac{1}{2}e\mathbf{Q}\colon (\nabla\boldsymbol{\psi}\nabla\boldsymbol{\psi}) + \frac{1}{2}b_1|\nabla\boldsymbol{\psi}|^2 + \frac{1}{4}b_2|\nabla^2\boldsymbol{\psi}|^2 \quad (2.6)$$

Considering Equation 2.6, assuming a spatially homogenous system, and performing reparameterization (see Supplementary Appendix A1), we find the following governing free energy density $F(\psi, S_A)$:

$$F(\psi, S_A) = \underbrace{\frac{1}{3}aS_A^2 - \frac{2}{27}bS_A^3 + \frac{1}{9}cS_A^4}_{F_N} + \underbrace{\frac{1}{2}\left(\alpha - \frac{b_1^2}{2b_2}\right)\psi^2 + \frac{1}{4}\beta\psi^4}_{F_S} \underbrace{-\left(\frac{e^2 + 3\delta b_2}{9b_2}\right)\left[S_A^2\psi^2 - \left(\frac{3eb_1}{(e^2 + 3\delta b_2)}\right)S_A\psi^2\right]}_{F_{NS}}, \quad (2.7)$$

where F_N is the nematic contribution, F_S is the smectic contribution, and F_{NS} is the crucial coupling contribution between the positional and orientational OPs that are in their expanded form. In this paper, we evaluate the OPs in their extended domain of dependence $F(\psi, S_A)\colon [-1, 1] \times [-1/2, 1] \to [-F_0, \infty)$ to fully capture the important phenomena at the nematic axis $(\psi = 0)$ and the smectic axis $(S_A = 0)$; we note that negative nematic OP states (molecular alignment normal to the director orientation) are usually considered in nematostatics (Golmohammadi and Rey, 2010), but in the particular equilibrium spatially homogeneous I-SmA transitions considered in this study, these orientation states play no role.

The possible states are obtained by the minimization of the homogeneous free energy in Equation 2.7 concerning the two non-conserved OPs (ψ, S_A). This yields a system of ODEs (see Supplementary Appendix A1). Then, at a given temperature T, different phases arise according to the ordering contributions. As mentioned in the introduction, positional and orientational ordering define an LC state, which varies in accordance with the combination of these order parameters. In this paper, we consider the following:

$$\begin{aligned} &\text{Isotropic (Iso)}\colon S_A = \psi = 0.\\ &\text{Nematic (N)}\colon S_A > 0, \psi = 0.\\ &\text{Plastic crystal (P}_c\text{)}\colon S_A = 0, \psi > 0.\\ &\text{Smectic} - \text{A (SmA)}\colon S_A > 0, \psi > 0. \end{aligned} \quad (2.8)$$

The isotropic-liquid state is characterized by the absence of positional and orientational orders, the nematic LC possesses only average molecular orientation, the plastic crystal phase (characterized by the density wave) describes a material with positional order and very small-to-none orientational order, and the smectic A LC exhibits positional and orientational orders (Oswald and Pieranski, 2005a; Oswald and Pieranski, 2005b; De Gennes, 2007; Demus et al., 2008a; DiLisi, 2019; Mukherjee, 2021). We note that the density wave behavior, designated as the plastic crystal state in this study, has been reported even for some rod-like systems (Kyrylyuk et al., 2011; Liu et al., 2014; Sato et al., 2023). In this work, the metastable plastic crystal emerges at deep quenches when the isotropic state becomes unstable, the nematic and coupling energies vanish, and the stable phase is SmA. Similarly, since $(e^2 + 3\delta b_2)/9b_2 > 0$ and $[S_A^2\psi^2 - (3eb_1/(e^2 + 3\delta b_2))S_A\psi^2] > 0$ for the SmA state in Equation 2.7, the important coupling term F_{NS} promotes the emergence of SmA with the positional and orientational order.

2.2 Geometric thermodynamics for phase ordering in the isotropic–smectic A transition

In this section, we investigate the surface geometry of the energy landscape $F(\psi, S_A)$, with a particular emphasis on understanding and characterizing the essential nature of all the critical points.

These critical points, derived from Equation 2.7, include the local maxima, local minima, and saddle points. As mentioned at the end of the introduction, their significance extends across many research fields in liquid crystals, such as self-assembly, kinematics, and thermodynamics of these systems.

Next, we briefly mention the basic argument to keep all critical points, forgoing complex mathematical details. For instance, the time-dependent Ginzburg–Landau model (Popa-Nita, 1999) provides a quantitative study of the spatiotemporal evolution of thermodynamic behaviors on a non-conserved OPs vector $\mathbf{p}$.

$$\frac{\partial \mathbf{p}}{\partial t} \propto \frac{\partial (f + f_e)}{\delta \mathbf{p}} = \frac{\partial (F + F_e)}{\partial \mathbf{p}} - \nabla \cdot \frac{\partial (F + F_e)}{\partial \nabla \mathbf{p}}, \mathbf{p} = \begin{bmatrix} \psi \\ S_A \end{bmatrix}, \quad (2.9)$$

where $F_e \propto \nabla \mathbf{p}$: $\nabla \mathbf{p}$ is the elastic energy dependent on the deformation; note that $\mathbf{p}$ is the OP vector for the smectic A phase. A special solution of Equation 2.9 describes a front propagation that could describe growing smectic droplets in an isotropic matrix. For example, the wave-like property has been intensively studied by De Luca and Rey (2004) for the case of chiral nematic fronts propagating into an unstable isotropic phase. In our present smectic model, the wave-like solution $\mathbf{p} = \mathbf{p}(\mathbf{x} - \mathbf{v}t) = \mathbf{p}(\tilde{\mathbf{x}})$; $\tilde{\mathbf{x}} = \mathbf{x} - \mathbf{v}t$ with constant velocity $\mathbf{v}$ simplifies Eq. 2.9 to a more compact form, $\frac{\partial F}{\partial \mathbf{p}} = (\mathbf{v} \cdot \tilde{\nabla} + \tilde{\nabla}^2)\mathbf{p}$, where all the coefficients are not included for clarity. At $\frac{\partial F}{\partial \mathbf{p}} = 0$, the critical points lay inside the kernel of the linear map defined by the velocity $(\mathbf{v} \cdot \tilde{\nabla} + \tilde{\nabla}^2)$. The polynomial decomposition of $F(\psi, S_A)$ (see Eq. 2.7 for the quartic polynomial expression in two variables (ψ, S_A)) then gives the governing equation for phase transformation, $(\mathbf{v} \cdot \tilde{\nabla} + \tilde{\nabla}^2)\mathbf{p} = \prod_i (\mathbf{p} - \hat{\mathbf{p}}_i)$, where $\hat{\mathbf{p}}_i$ are the critical points at critical points $(\partial_\psi F = \partial_{S_A} F = 0)$ and $\prod_i (\mathbf{p} - \hat{\mathbf{p}}_i)$ is the product function that expresses the polynomial $F(\psi, S_A)$. The phase transformation depends on the polynomial decomposition of the free energy involving all the critical points. Given the significance of all the critical points on growth, kinematics, and interfaces, we explore their behavior in this section.

2.2.1 Polynomial index theorem and critical points of the $F(\psi, S_A)$-energy landscape

Since the two-OP model considered in this study is of quartic order in each of the parameters, a proliferation of critical points and a complex energy landscape are expected. Hence, tools that set upper limits on the number and type of critical points are essential to achieving or enhancing tractability. In this section, we formulate an approach tailored to the I-SmA transition, keeping the complex mathematics to a minimum.

Let $\mathrm{f}(x, y)$ be a polynomial of degree $d > 1$. Then, f has a critical point (x_0, y_0), if $\partial_k \mathrm{f}(x_0, y_0) = 0$, where the following notation (∂_k) is adopted for partial derivatives of a given function with respect to k. The number of critical points N_{cp} is then defined by $(d-1)^2$. In general, for a given polynomial h in two variables x, y of degree d_x and d_y, respectively, we expect at most $d_x d_y$ critical points (Durfee et al., 1993). Thus, the computation of ψ and S_A from the solution of the ODEs (see Supplementary Appendix A2) that minimize the free energy F will yield at most $N_{\mathrm{cp}} = 9$ critical points and at least one critical point $N_{\mathrm{cp}} = 1$. These points include the degenerate and nondegenerate points that follow the well-known nondegeneracy criteria, which are as follows:

$$\partial_{\psi\psi}(F(\psi, S_A)) > 0, \ \partial_{SS}(F(\psi, S_A)) > 0, \quad (2.10)$$

$$\det \begin{bmatrix} \partial_{\psi\psi}(F(\psi, S_A)) & \partial_{\psi S}(F(\psi, S_A)) \\ \partial_{S\psi}(F(\psi, S_A)) & \partial_{SS}(F(\psi, S_A)) \end{bmatrix} \neq 0. \quad (2.11)$$

The number of critical points N_{cp} is bound by the Poincaré–Hopf index theorem (Knill, 2012). The index i_{f} of the gradient vector $\nabla \mathrm{f}$ is computed based on the nondegeneracy of all critical points of f, which assigns a value of (+1) to a maximum or minimum and a value of (−1) to a saddle (Durfee et al., 1993) in the following definition:

$$\begin{aligned} i_{\mathrm{f}} &= N_{\mathrm{maxima}} \times (+1) + N_{\mathrm{minima}} \times (+1) + N_{\mathrm{saddles}} \times (-1) \\ &= N_{\mathrm{maxima}} + N_{\mathrm{minima}} - N_{\mathrm{saddles}}. \end{aligned} \quad (2.12)$$

Here, the index of the free-energy polynomial of Equation 2.7 was computed as $i_F = +1$ in an area homeomorphic to a disk, which importantly puts a cap on the number of saddles N_{saddles}. Thus, from the index theorem, we conclude that saddles play a crucial role in this transformation across various temperature ranges.

2.2.2 Level-set and steepest descent

In addition to the index $i_F = +1$, the gradient vector $\nabla \mathrm{f}$ stores the information required to compute the directional derivative of $\mathrm{f}(x, y)$ for any direction at any point (x_i, y_i), which provides the rate of change in f as it approaches (x_i, y_i). This directional derivative is just the inner product of the gradient and the direction of a certain vector $\mathbf{u}$:

$$D_u \mathrm{f}(x, y) = \nabla \mathrm{f}(x, y) \cdot \mathbf{u}(i, j). \quad (2.13)$$

The gradient then contains the direction of the greatest change of f, known as the steepest descent, or ascent, as the opposite direction that may be computed with $-\nabla \mathrm{f}$. Contrary to this, a vector orthogonal to $\nabla \mathrm{f}$ will point toward a zero change in f. These are vectors that lie on the tangent plane and are normal to a surface that can be constructed by the level set of the scalar-valued function $\mathrm{f}: \mathbb{R}^n \to \mathbb{R}$. These are cross-sections of the (x, y)-frame, individually representing its different levels c and containing any real solution of $\mathrm{f}(x, y)$.

$$\{(x, y) \in \mathbb{R}^2 \mid \mathrm{f}(x, y) = c\}. \quad (2.14)$$

The energy landscape $F(\psi, S_A)$ is a surface whose main features are characterized by the shape of the level-set curves, the direction of the steepest descent curves, and the location and nature of the critical points. For a given set of critical point locations, the level sets and steepest descent indicate how and if local minima can be reached. For example, local minima (maxima) on the energy surface are characterized by ellipses, and the steepest descent curves are converging (diverging) splay curves (see Figure 2). This is similar to the minimum energy path (MEP) approach (Massi and Straub, 2001; Liu et al., 2022), which seeks to locate and characterize the conformation changes between chemical states based on their relationship with their characteristic energy hypersurface (Fischer and Karplus, 1992; Wang et al., 1996; Liu et al., 2022) that describes the thermodynamic equilibrium and self-assembly process.

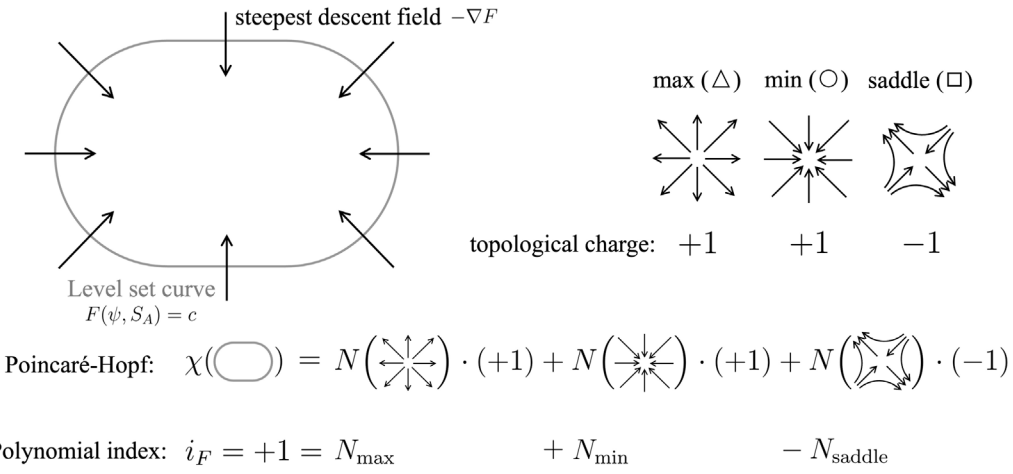

FIGURE 2
Schematic of the first family of the free-energy landscape $\boldsymbol{F}(\psi, S_A)$: level-sets, steepest descent, and polynomial index (Sections 2.2.1–2) and their relationship. The symbols on the top right are kept throughout the paper to designate the nondegenerate points: maximum, minimum, and saddle. The polynomial index is then computed based on the topological charge assigned to these points. The representation of the local steepest gradient field is included for each point. Here, χ denotes the Euler characteristic of the area enclosed by the level-set curve.

Figure 2 presents the connection between the polynomial index and the level set and steepest descent curves. By assigning topological charges to the critical points based on their nondegeneracy, the polynomial index is constructed. Each nondegenerate point is then linked to the expected local behavior of the gradient vector.

2.2.3 Lines of curvature and geodesics

The lines of curvature are computed by solving a set of equations defined by the coefficients of the first (**g**) and second (**b**) fundamental forms, as shown in Supplementary Appendix A2 (Maekawa, 1996; Farouki, 1998). The LOC have been used to describe the relationship between entropy production in membranes and interfaces (Wang et al., 2020) and the curvature of isotropic–smectic interfaces under self-organization (equilibrium) and self-assembly (dynamic) states (Vitral et al., 2019) using an orthonormal network. These LOC applied to the free-energy landscape describe the change in the order parameters with respect to the arc-length s, following the principal direction of the tangent vectors (Eq. A.6) along γ: $\mathrm{d}\gamma/\mathrm{d}s = \mathbf{r}_k/\|\mathbf{r}_k\|$, where γ is a line of curvature. Thus,

$$\frac{\mathrm{d}\psi}{\mathrm{d}s} = \eta(M - \kappa A) \quad \text{and} \quad \frac{\mathrm{d}S_A}{\mathrm{d}s} = -\eta(L - \kappa E), \tag{2.15}$$

or

$$\frac{\mathrm{d}\psi}{\mathrm{d}s} = \mu(N - \kappa G) \quad \text{and} \quad \frac{\mathrm{d}S_A}{\mathrm{d}s} = -\mu(M - \kappa A), \tag{2.16}$$

where κ represents the principal curvatures (κ_1, κ_2), (E, A, G), and (L, M, N) are the coefficients of the first and second fundamental forms (see Supplementary Appendix A2) and (η, μ) are non-zero coefficients defined by

$$\begin{aligned} \eta &= \left(E(M - \kappa A)^2 - 2A(M - \kappa A)(L - \kappa E) + G(L - \kappa E)^2\right)^{-1/2} \\ \mu &= \left(E(N - \kappa G)^2 - 2A(M - \kappa A)(N - \kappa G) + G(M - \kappa A)^2\right)^{-1/2}, \end{aligned} \tag{2.17}$$

$$\mathrm{d}s = \sqrt{E(\mathrm{d}\psi)^2 + 2A\mathrm{d}\psi\mathrm{d}S_A + G(\mathrm{d}S_A)^2}. \tag{2.18}$$

Under our free-energy framework $F(\psi, S_A)$, the geodesic lines indicate the shortest path between two points in the thermodynamic equilibrium state (Do Carmo, 2016; Wang et al., 2020), which can also show the self-assembly path connecting the phases expected in the I-SmA energy landscape. This is similar to what is found in the analysis of the geometry of thermodynamic stable states of ideal gases (Quevedo et al., 2008). This is described by a curve with the smallest arc length connecting two points on a given surface, and it is given by the following equation (Do Carmo, 2016; Wang et al., 2020):

$$\frac{d^2 y^k}{ds^2} + \Gamma_{ij}^k \frac{dy^i}{ds}\frac{dy^j}{ds} = 0, \tag{2.19}$$

where E, A, and G are the first fundamental form coefficients, Γ_{ij}^k are the Christoffel symbols, and the geodesic curve is y^i for the ith component of the quantities that define the free-energy parametrized surface (ψ, S_A) (see Supplementary Appendix A3).

2.2.4 Casorati curvature and shape coefficient

In this section, we provide details of the Casorati curvature (C) and shape coefficient (S) given in the introduction and Figure 1 (lower left vertex). A method presented by Wang et al. (2020) redefines a thermodynamic hypersurface into a Monge shape-curvedness surface patch for the characterization of entropy production in LC membranes and interfaces. As mentioned above, in this paper, we use this methodology to describe the local geometry of the I-SmA phase transition energy landscape using a normalized shape coefficient (S) that distinguishes between three primary shapes: cup/cap (spherical), rut/ridge (cylindrical), and saddle, and the Casorati curvature (C) for the curvature magnitude measurement (Koenderink and van Doorn, 1992; Aguilar Gutierrez and Rey, 2018). This requires the reparameterization of the energy landscape $F(\psi, S_A)$ into a

Monge patch (Abbena et al., 2017) comprised of the shape coefficient (S) and Casorati curvature (C).

Classical curvature concepts, in addition to the Casorati curvature (C) and shape coefficient (S) (Wang et al., 2023a), are used in the description of the curvedness and shape, such as the (i) mean (H), (ii) deviatoric (D), and (iii) Gaussian (K) curvature (see Supplementary Appendix A2), whose information is stored in the surface gradient of the surface unit normal $-\nabla_s \mathbf{k}$, where $\nabla_s = (\mathbf{I} - \mathbf{kk}) \cdot \nabla$ is the surface gradient and ∇ is the gradient operator. From this, the symmetric curvature tensor is defined as $\mathbf{b} = -\nabla_s \mathbf{k} = \kappa_1 \mathbf{e}_1 \mathbf{e}_1 + \kappa_2 \mathbf{e}_2 \mathbf{e}_2$, where (κ_1, κ_2) are its eigenvalues (see Figure 1II) characterizing the principal curvatures (Aguilar Gutierrez and Rey, 2018). The Casorati curvature is defined by $C = \sqrt{(\kappa_1^2 + \kappa_2^2)/2}$, the mean curvature by $H = (\kappa_1 + \kappa_2)/2$, the deviatoric curvature by $D = (\kappa_1 - \kappa_2)/2$, and the Gaussian curvature by $K = \kappa_1 \kappa_2$, for which the principal curvatures are assumed to follow $\kappa_1 \geq \kappa_2$ (Wang et al., 2020).

The non-dimensionality of the shape coefficient condenses information that allows it to classify the local shape into simple geometries within the normalized range $S \in [-1, +1]$. The Casorati curvature, however, quantifies how curved a surface is (Aguilar Gutierrez and Rey, 2018; Wang et al., 2020) (see Supplementary Appendix A2)

$$S = \frac{2}{\pi} \arctan\left(\frac{H}{D}\right) \quad \text{and} \quad C = \sqrt{2H^2 - K}. \tag{2.20}$$

The primary fundamental shapes are then generalized with $S = \{0, \pm 1/2, \pm 1\}$, assigning the values to a saddle (0), a rut ($-1/2$), a ridge ($+1/2$), a cup (-1), and a cap ($+1$), where the $\pm$ sign defines if it is a concave-up (negative) or concave-down (positive) patch (see Figure 1.III). It is important to notice that these are primary shapes and a continuous spectrum is contained within the normalized parameter interval. The Casorati curvature varies within $C = [0, +\infty)$, defining a flat surface with no curvature ($C = 0$) and a curved surface ($C > 0$), respectively. Figure 1 (III) shows a schematic representation of the Casorati curvature (upper set) and the shape coefficient spectrum (lower set).

2.3 Computational methods

In this work, we sought detailed information of the phase ordering as the quenching degree increases from the highest possible temperature for the existence of the SmA phase. We found that it is possible to classify the ordering and geometry by defining three quenching regimes: shallow quench, middle quench, and deep quench (with three temperatures corresponding to each of them, as listed in Table 2). As the degree of quenching increased, the isotropic phase lost stability, while the SmA gained stability, and a number of saddle nodes and supercritical bifurcations emerged at the boundaries of these quench regimes. Given the nonlinearities and OP couplings in the energy density and the differential geometry quantities, high-performance computational techniques were developed, applied, and tested when exact data were available, and high fidelity was demonstrated. Stability, accuracy, and dispersion criteria were implemented according to the standard numerical methods. The validation of our results was established using previous studies (Urban et al., 2005; Abukhdeir and Rey, 2008; Coles and Strazielle, 2011). As mentioned in the introduction, a well-characterized member of the n-cyanobiphenyl family (12CB) has been chosen as the study case for its I-SmA transition behavior (see Supplementary Appendix A4).

The calculation sequence was as follows: (1) level sets and steepest descent curves were obtained with (i) the complete solution of Equation 2.7 at different temperatures for the phases in Equation 2.8 using the stability criteria in Section 2.2.1, which categorizes the critical points that are bound by the number N_{cp} and the I-SmA LdG free-energy index i_F in Equation 2.12 and (ii) the orthogonal pair of steepest descent and level-set curves from Section 2.2.2. (2) Geodesics/LOC calculations in Section 2.2.3 involved coupled nonlinear second-order stiff ODEs, which are numerically unstable depending on the step size taken, especially the system of equations defined by the discretization of the geodesics (Equation 2.19) (see Supplementary Appendix A2). Boundary conditions must be provided to solve the geodesic. We used the shooting method, which requires the definition of a starting point, chosen in our case study to be the stable isotropic/smectic A phases. In addition to equation stiffness, it is also worth noting that the model is arc-length parametrized, meaning that the arc length was computed for every step. In the LOC case, the sets of Equations 2.15–2.16 while seeming analogous, are in reality distinct instances of the principal directions that depend on the arc length. The sign of the proceeding direction at a given point $(\psi_n, S_{A,n})$ must be adjusted according to the local surface geometry, meaning that the system solved was switched from one to another depending on the maximum and minimum principal curvatures (κ_1, κ_2) (Farouki, 1998; Wang et al., 2020). For this, we followed a very robust algorithm developed for computing LOC (Maekawa, 1996; Farouki, 1998), which generates a pair of orthogonal curves at $(\psi_n, S_{A,n})$ following the criterion: Equation 2.15 is solved if $|L - \kappa E| \geq |N - \kappa G|$, and Equation 2.16 is used otherwise. Then, a curvature network was constructed with the orthogonal LOC by solving the ODE system at a point $(\psi_n, S_{A,n})$ along the length defined by the energy landscape for a sufficiently small step-size that balances out resolution, solution stability, and computational time. (3) For obtaining the Casorati and shape coefficient in Section 2.2.4, we computed the first fundamental forms and the principal curvatures of the free-energy landscape (see Supplementary Appendix A2).

3 Results and discussion

In this paper, we present a complete description and characterization of the energy landscape of the isotropic–smectic A transition using a two-non-conserved order parameter version of the Landau–de Gennes model for the following reasons: (i) the kinetics of phase transformations for non-conserved order parameters is dependent on stable, metastable, and unstable critical points of free energy (Tuckerman and Bechhoefer, 1992; De Luca and Rey, 2003; De Luca and Rey, 2004); this point is briefly elaborated at the beginning of Section 2.2; (ii) in the case of phase transformation by propagating fronts, where a stable phase replaces an unstable phase, non-monotonic ordering structures appear at the interface due to the presence of various critical points (Tuckerman and Bechhoefer, 1992); (iii) in the case of drop formation of a stable

phase in a metastable matrix, one can expect thin film-like layers with intermediate degrees of order between the droplet phase and matrix (Abukhdeir and Rey, 2009a); (iv) interfacial processes as in a LC drop couple shape-bulk and surface structure-size due to orientational order (Rey, 2000; Rey and Denn, 2002; Rey, 2004a; Rey, 2004b; Rey, 2006). In view of these phenomena, we do not neglect metastable and unstable ordering states, such as nematic or plastic (density wave) phases, as previously suggested (Saunders et al., 2007). How exactly they will manifest themselves under nucleation and growth and spinodal transformation of the isotropic phase into the SmA phase will be examined in future work and is outside the scope of this paper.

3.1 Quench zones and critical points and their stability

Figure 3 presents the orientational and positional order phase diagram as a function of temperature T obtained by solving Equation 2.7 with 12CB material parameters (Supplementary Appendix A4). Subscripts on the OPs denote stable (s), unstable (u), and metastable (m); superscripts denote larger (+) and smaller (−) values. The line style (full, dashed, and doted) identifies the phase (see Eq. 2.8). The figure frames the three quenches (see Table 2) delimited by key temperatures: the deep quench for $T < T_{SD}$ (light blue), the middle quench for $T_{SD} < T < T_{NG}$ (light purple), and the shallow quench for $T < T_{IL}$ (light red). Here, T_{SD} is the spinodal decomposition temperature, T_{NG} is the nucleation and growth temperature, and T_{IL} is the maximum temperature for the existence of any smectic order phase, as explained below. Using quenching measures, we can characterize the critical point features and determine whether they are stable, unstable, or metastable, depending on the quench zone. To fully characterize the nature of all the sources and sinks at the nematic axis $(S_A > 0, \psi = 0)$, we include $\psi < 0$ solutions. These non-physical solutions $(S_A > 0, \psi < 0)$ arise from the mirror symmetry of the free energy $F(S_A, \psi) = F(S_A, -\psi)$ but assist in characterizing transitions and bifurcations that occur at the $S_A = 0$ axis. In describing and classifying results, we focus on the I-SmA transition, and the quench depth refers to a temperature decrease from the highest temperature (T_{IL}) at which the metastable SmA arises. Thus, reference to nucleation and growth mode, NG, indicates the temperature interval in which the isotropic (SmA) phase is metastable (stable), and when referring to spinodal decomposition, SD, the isotropic (SmA) phase is unstable (stable). The challenges regarding the location of the critical points at a given quench, their stability, and the other possible states when considering the entirety of the points, which were introduced at the beginning of the paper, are addressed below.

The phases in the deep quench (light blue region in Figure 2) to the spinodal decomposition region are the following:

- $S^{+}_{A,s}, \psi^{+}_{s}$ stable SmA black, continuous lines.
- Iso_u unstable isotropic, red-dotted line.
- $S^{-}_{A,u}, \psi^{-}_{u}$ unstable nematic/smectic, black, dashed lines.
- N^{+}_{u}, N^{-}_{u} unstable nematic, blue, dashed lines.
- $\psi^{+}_{u}, \psi^{-}_{u}$ unstable smectic, gray, dash-dotted lines.
- P^{+}_{m}, P^{-}_{m} metastable plastic crystal, purple, dash-dotted lines.

Here, the SD region exhibits an unstable isotropic state and a stable SmA. In addition, we find a metastable plastic region. This region exists for $T < T_{SD} = 330.6$ K. Thus, we expect that quenching an isotopic phase into the spinodal region will transform the phase into a stable SmA phase, but the presence of unstable smectic and metastable plastic crystal states introduces complexities to the energy landscape.

The phases in the middle quench (light purple region in Figure 2) to the nucleation and growth region are the following:

- $S^{+}_{A,s}, \psi^{+}_{s}$ stable SmA, black, continuous lines.
- Iso_m metastable isotropic, red-dotted line.
- $S^{-}_{A,u}, \psi^{-}_{u}$ unstable nematic/smectic, black, dashed lines.
- N^{+}_{u}, N^{-}_{u} unstable nematic, blue, dashed line.
- $\psi^{+}_{u}, \psi^{-}_{u}$ unstable smectic, gray, dash-dotted line.

In the ND region, the isotropic state is metastable and SmA is stable, as in the SD region, in addition to the unstable smectic and nematic phases. However, the density wave is no longer present as it vanishes at the temperature T_{SD}, and the isotropic phase becomes metastable. This region exists $T_{SD} = 330.6\,\text{K} < T < T_{NG} = 331.3\,\text{K}$. Thus, we expect that quenching an isotropic phase into the NG region will transform the phase into a stable SmA phase by droplet growth.

The phases in the shallow quench (light red region in Figure 2) are the following:

- $S^{+}_{A,m}, \psi^{+}_{m}$ metastable SmA, black, continuous lines
- Iso_s stable isotropic, red-dotted line.
- $S^{-}_{A,u}, \psi^{-}_{u}$ unstable nematic, black, dashed line.
- $\psi^{+}_{u}, \psi^{-}_{u}$ unstable smectic, gray, dash-dotted line.

At shallow quenches, the isotropic phase is now stable, while SmA is only metastable. In addition, the unstable smectic state remains, but the nematic loop closes and vanishes at the temperature T_{NG}. This region is then defined by $T_{NG} = 331.3\,\text{K} < T < T_{IL} = 331.85\,\text{K}$. Quenching from the NG triggers a phase transition at temperature T_t, as obtained with the solution of Equation 2.7 for a temperature at which $F = F_0$; thus, a temperature higher than the isotropic limit T_{IL} will lead to a disordered state.

The deep quench is characterized by the strong stability and presence of the expected smectic A phase and by a supercritical bifurcation (Oswald and Pieranski, 2005a) or plastic loop since it belongs to the metastable plastic crystal phase, where mirror symmetry is broken at the temperature T_{SD}. The nematic order effect is seen in the orientational order parameter diagram, with the presence of the nematic loop in the deep- and middle-quench zones. This marks the entrance of the shallow quench and the stability change of the SmA phase. A summary of these key temperatures and regions is given in Table 1.

The computed energy landscape has a critical root population that decreases exactly as predicted by the polynomial index theorem (Eq. 2.12; Figure 2) as the temperature increases. This is summarized in Table 2, where the number of nondegenerate points is included along with their type and the index value for each quench zone (see (2.12)).

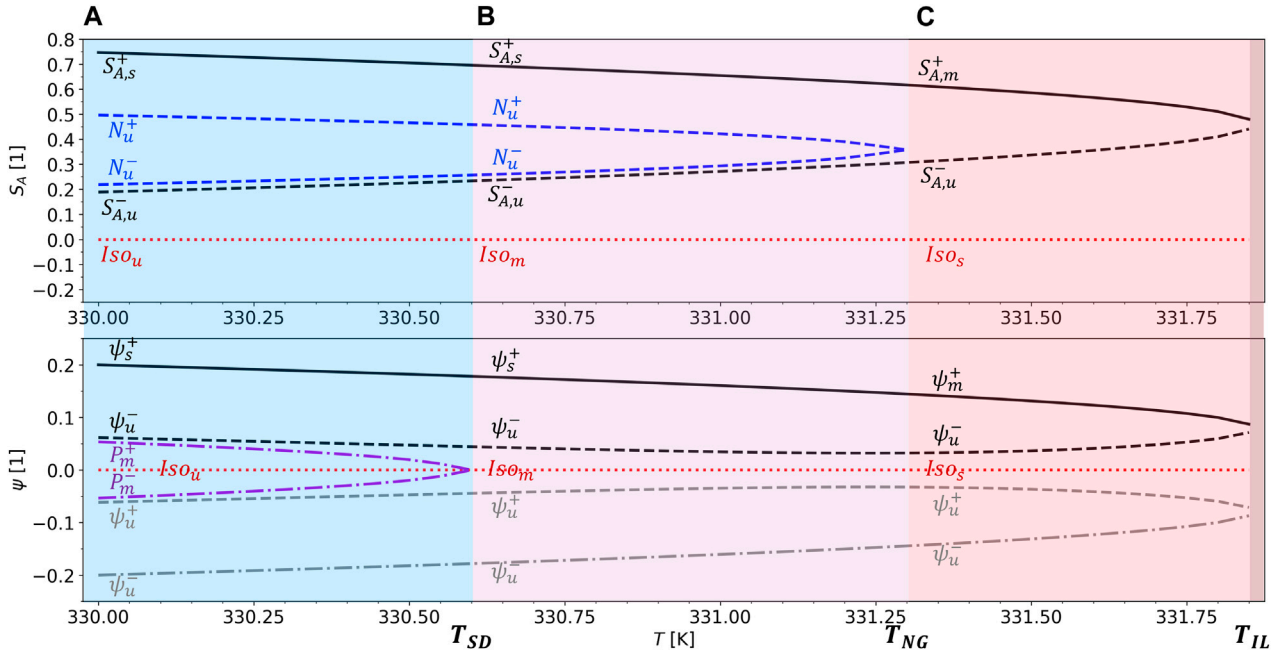

FIGURE 3
Positional ψ_n and orientational $S_{A,n}$ order parameters of the isotropic (*Iso*) to SmA phase transition for 12CB as a function of temperature with all the critical points: sub-index $\boldsymbol{n} = (s, m, u)$ refers to stable, metastable, and unstable, respectively. The three different zones correspond to three different quenches: **(A)** deep quench (DQ), **(B)** middle quench (MQ), and **(C)** shallow quench (SQ). Derived from the LdG model (Eq. 2.7). The material parameters used (Urban et al., 2005; Abukhdeir and Rey, 2008; Coles and Strazielle, 2011) are as follows: $a_0 = 2 \cdot 10^5 \text{J}/(\text{K m}^3)$, $b = 2.823 \cdot 10^7 \text{J/m}^3$, $c = 1.972 \cdot 10^7 \text{J/m}^3$, $\alpha_0 = 1.903 \cdot 10^6 \text{J}/(\text{K m}^3)$, $\beta = 3.956 \cdot 10^8 \text{J/m}^3$, $\delta = 9.792 \cdot 10^6 \text{J/m}^3$, $e = 1.938 \cdot 10^{-11} \text{J/m}$, $b_1 = 1 \cdot 10^{-11} \text{J/m}$, $b_2 = 3.334 \cdot 10^{-30} \text{J/m}$, $d_0 = 2\pi/(3.9 \cdot 10^9 \text{ m})$, $T_{NI}^{*} = 322.85 \text{ K}$, and $T_{AI}^{*} = 330.5 \text{ K}$. The results are fully consistent with Figure 4 of Abukhdeir and Rey (2008). Key temperatures: T_{SD}, T_{NG}, and T_{IL} are listed in Table 2.

TABLE 1 Summary of stable, unstable, and metastable states in each quench zone and their key temperatures as presented in Figure 2.

	Deep Quench (DQ): Spinodal Decomposition for the Isotropic phase.	Middle Quench (MQ): Nucleation and Growth for the Isotropic phase.	Shallow Quench (SQ): Limit for the Isotropic phase.	Zero quench
Primary roots	Stable smectic A Unstable isotropic	Stable smectic A Metastable isotropic	Metastable smectic A Stable isotropic	Stable isotropic
Secondary roots	Metastable plastic crystal Unstable nematic Unstable smectic A	Unstable nematic	NA	NA
Transition temperature	$T_{\text{SD}} = 330.6 \text{ K}$	$T_{\text{NG}} = T_t = 331.3 \text{ K}$	$T_{\text{IL}} = 331.85 \text{ K}$	

TABLE 2 Number and types of critical points on the phase diagram for different temperatures and their indexes; the three cases presented in Figure 2 correspond to the three quench zones; and one for the complete isotropic phase transition. The symbol style used for each of them is kept constant throughout the paper. Numerical results are in exact agreement with the polynomial index theorem (Eq. 2.12).

T [K]	Maxima	Minima	Number of saddles	Index i_F	Zone
A–330	1	4	4	1	Deep quench (spinodal decomposition, SD)
B–331	1	3	3	1	Middle quench (nucleation and growth, NG)
C–331.85	0	3	2	1	Shallow quench
$T > T_{\text{IL}}$	0	1	0	1	
Symbol in Figure 3	Δ	○	□		

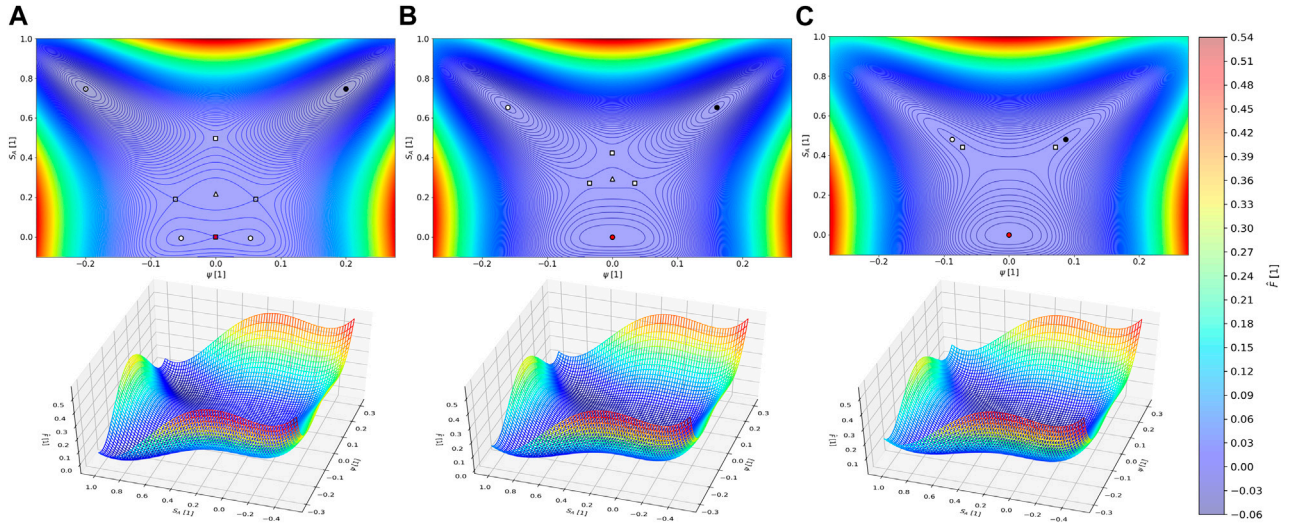

FIGURE 4
Energy landscape constructed with the positional (ψ) and orientational (S_A) order parameters of the I-SmA phase transition for 12CB (see Figure 3, and Supplementary Appendix A4) and the dimensionless free energy ($\hat{F}$) at the three temperatures **(A–C)** included in Table 2. The LDG model was nondimensionalized for visualization purposes with the orientational temperature-dependent parameter a. The critical points are included for each scenario. The temperatures, which belong to each quench zone, and the markers are listed in Table 2, indicating the stability type assigned based on the criteria given by Eqs 2.10–2.11. The black and red markers indicate the primary roots: SmA and isotropic state, respectively. $\hat{F}$ ranges in the color bar are kept the same throughout the paper. The 3D plots of the same energy landscapes are included right below each one for the same temperatures for a more complete view.

The bounds in Equations 2.10–2.11 provide stability boundaries that do not necessarily mean a phase transition line but present the possible real physical phases that can be displayed within that range given the first-order nature of this transition (Mukherjee et al., 2001). Thus, the phase transition line was found by looking for a metastability–stability exchange of the I-SmA phases using level sets and computing the temperature at which both phases present the same energy level. This temperature, T_t, happened to be around the limit at which the nematic unstable loop vanished, going from deep quench (DQ) to middle quench (MQ), as seen in Figure 2, agreeing with the experimental transition temperature of 331.3 K (Coles and Strazielle, 2011).

Figure 4 represents the $\hat{F}(\psi, S_A)$ dimensionless free-energy landscape 2D projection for the LdG model using the parameters in Figure 2, with its corresponding 3D energy landscape at a given temperature. We have expanded the x-axis to negative values to emphasize the mirror symmetry along the positional order. The level-set curves have been included with all the critical points at three different temperatures in Table 2, which are representative of each quench zone. As quench depth decreases (temperature increases), the critical point population density decreases ($N_{cp} \downarrow$), which corresponds to the merging and vanishing of the nondegenerate points, as seen in Figure 2. Increasing T from the spinodal region, the plastic loop eventually converges at a supercritical bifurcation (Han and Rey, 1993; Rey, 1995) at T_{SD}, which is a process that replaces two minima (+2) and one saddle (−1) with a single minimum (+1). Entering the NG quench region with three saddles and four nodes (i.e., maximum or minimum), a further increase in T eventually leads to saddle-node bifurcation (Rey, 1995), with the elimination of a nematic saddle and a node. The shallow quench now has three minima and two saddles, which, after another saddle-node bifurcation of smectic phases, eventually leads to a planar surface with no order. It is noteworthy that the sequence of saddle number elimination as T increases and order decreases is multi-stepwise: $4 \rightarrow 3 \rightarrow 2 \rightarrow 0$. Likewise, the sequence of local minima elimination as T increases and order multi-stepwise decreases is $4 \rightarrow 3 \rightarrow 3 \rightarrow 1$. On the other hand, the elimination of the maxima follows a single step: $1 \rightarrow 1 \rightarrow 0 \rightarrow 0$. This shows that for shallow quench, local maxima play no role, and for deep quench, saddles and minima are equal in number.

3.2 Level-set curves and steepest descent lines

Figure 5 presents the level-set curves and the steepest descent lines (see Section 2.2.2), including the critical points projected on the dimensionless energy surface $\hat{F}(\psi, S_A)$ for the three quench regimes listed in Table 1. The blue (red) region corresponds to lower (higher) energy. It is seen that the steepest descent and level-set curves are members of an orthogonal family, where the level-set curves indicate a constant free-energy value and the steepest descent presents a path leading to primary roots that come from the minimization of the LdG model. The pair of roots (isotropic and smectic A phases) are divided by a set of maximums, minima, and saddles that discretely disappear as the quench depth decreases. In the deep-quench region, (A) the main feature is the family of elliptical rings around the stable SmA state (black dot), whose largest axes are oriented toward the

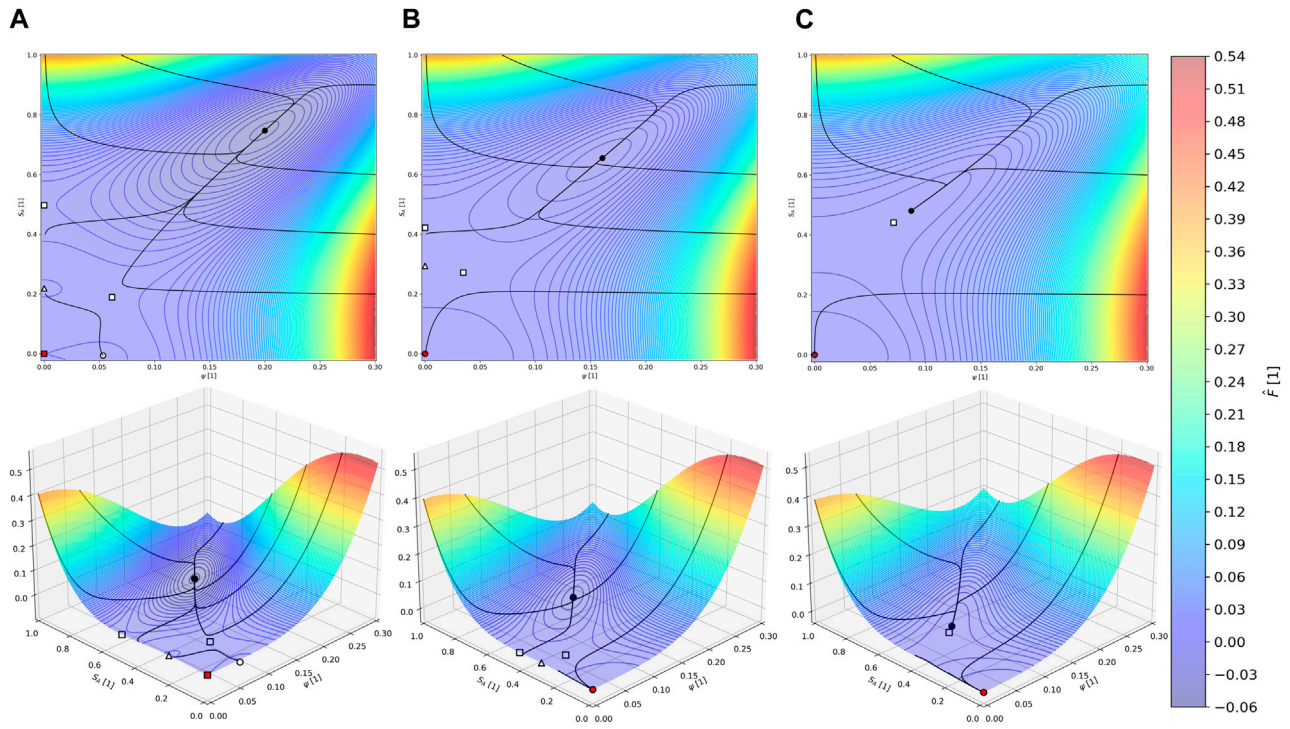

FIGURE 5
(ψ, S_A)-energy landscape with level-set, steepest descent curves, and critical points for $0 \le \psi \le 0.3$ and $0 \le S_A \le 1$, and the dimensionless free energy $\hat{F}$ levels, at the same parameters from FIGURE 3. The three temperatures used **(A–C)** and the marker styles are listed in Table 2. The continuous black lines go along the steepest descent and perpendicularly to the level-set curves that mark different free-energy levels. The black- and red-filled markers correspond to the SmA and isotropic states, respectively. A zoomed-in plot around the SmA is included for (b).

unstable phases. The level sets identify the nematic saddle and nematic maximum as well as the metastable plastic root. The principal steepest descent line connects the unstable smectic (white square) with the stable isotropic state (black dot) and defines a collecting manifold with nearly horizontal, constant S_A values. In the middle quench, nucleation, and growth, (B) the region of elliptical trajectories surrounding the SmA phase moves toward the isotropic state, causing the horizontal band of steepest descent lines to narrow. Furthermore, the steepest descent inverted L shows how energy states near the energetically high region end at the isotropic state (red dot). In (C), the metastability of SmA is shown by a lack of elliptical trajectories and the stability of the isotropic state.

In partial summary, the level-sets/steepest descent lines show the main features of the energy landscape; the number, location, and type of critical points; and the basin of attraction of SmA under spinodal and nucleation and growth conditions.

3.3 Lines of curvature and geodesics

Figure 6 shows the 2D projection and 3D plot of the LOC network on the energy landscape $\hat{F}(\psi, S_A)$ generated with the algorithm described in Section 2. It consists of orthogonal curve pairs that follow the minimum and maximum curvatures (cyan and magenta, respectively) at a given point on the surface. It also includes the primary roots shown in Table 1.

The maximum curvature (magenta) lines on the top left and bottom right closely follow the energy contours, corresponding to high S_A–low ψ and *vice versa*, while along the downward diagonal, they funnel out consistently in accordance with the energy landscape. The minimum curvature (cyan) lines form a set of nearly parallel L-lines, which are nearly vertical along the nematic axis and nearly horizontal close to the smectic axis. This is consistent with the fact that most critical points are around the diagonal region, as shown in Figure 5. Furthermore, since the energy surface envelope is roughly a concave-up expanding cylinder with flat edges, it follows that we must find circular curvature lines (as in the circular lines of a cylinder) and diverging straight lines (like in an expanding cone).

Figure 7 shows the projected geodesic lines of the energy landscape, computed by solving Equation 2.19 for the temperatures belonging to the three quench zones listed in Table 1 with the method provided in Supplementary Appendix A2. The geodesic family origin is the isotropic state that changes stability from unstable (A) to metastable (B) to stable (C), as seen in Figure 4. The lines minimize the path length and are therefore significant directions for phase changes. These lines show an expanding funnel whose centerline (purple) connects the two primary I-SmA phases. This line, which resembles the MEP introduced in Section 2.2.2, follows the minimum-curvature tendency designated in Figure 6 by the magenta lines. In addition, this phase-connecting geodesic becomes straighter as the depth quench is increased, achieving essentially a straight line

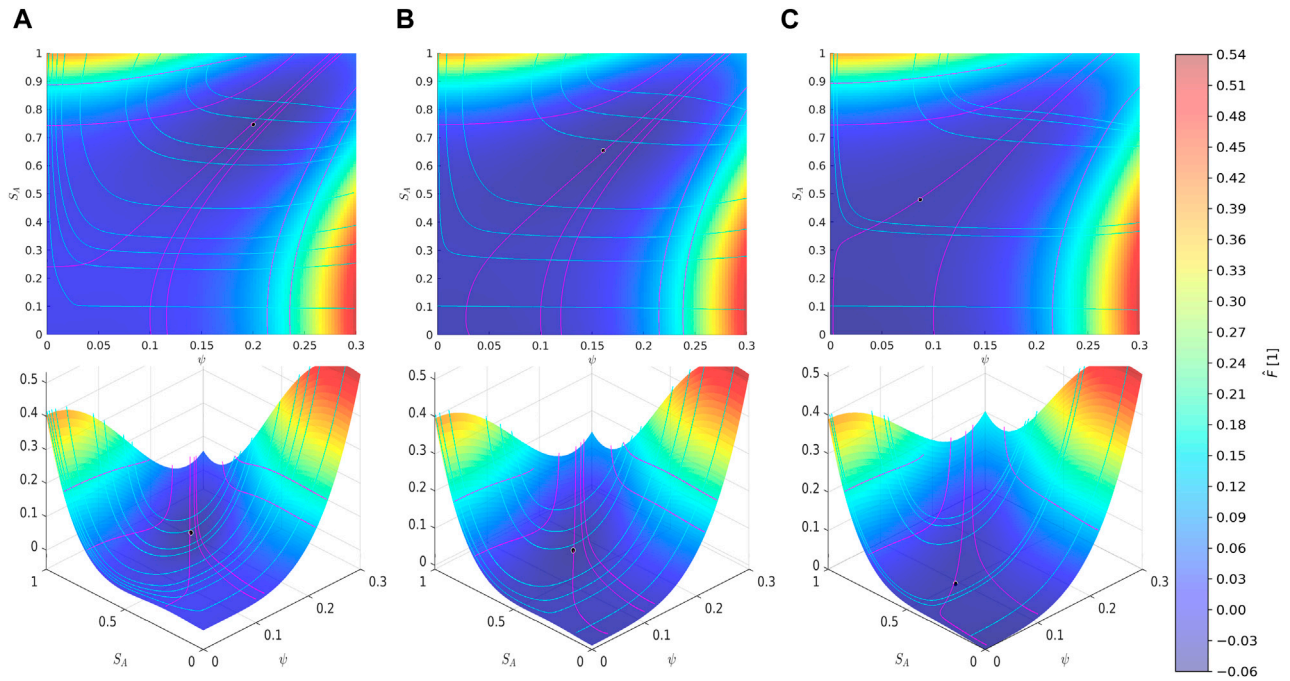

FIGURE 6
Lines of curvature projected on the (ψ, S_A)-energy landscape at the same three temperatures **(A–C)** and with the marker styles listed in Table 2. The parameters used are listed in Figure 3. The circular marker presents the SmA state at those temperatures. The cyan and magenta orthogonal network of LOC corresponds to the minimum κ_1 and maximum κ_2 curvatures, respectively.

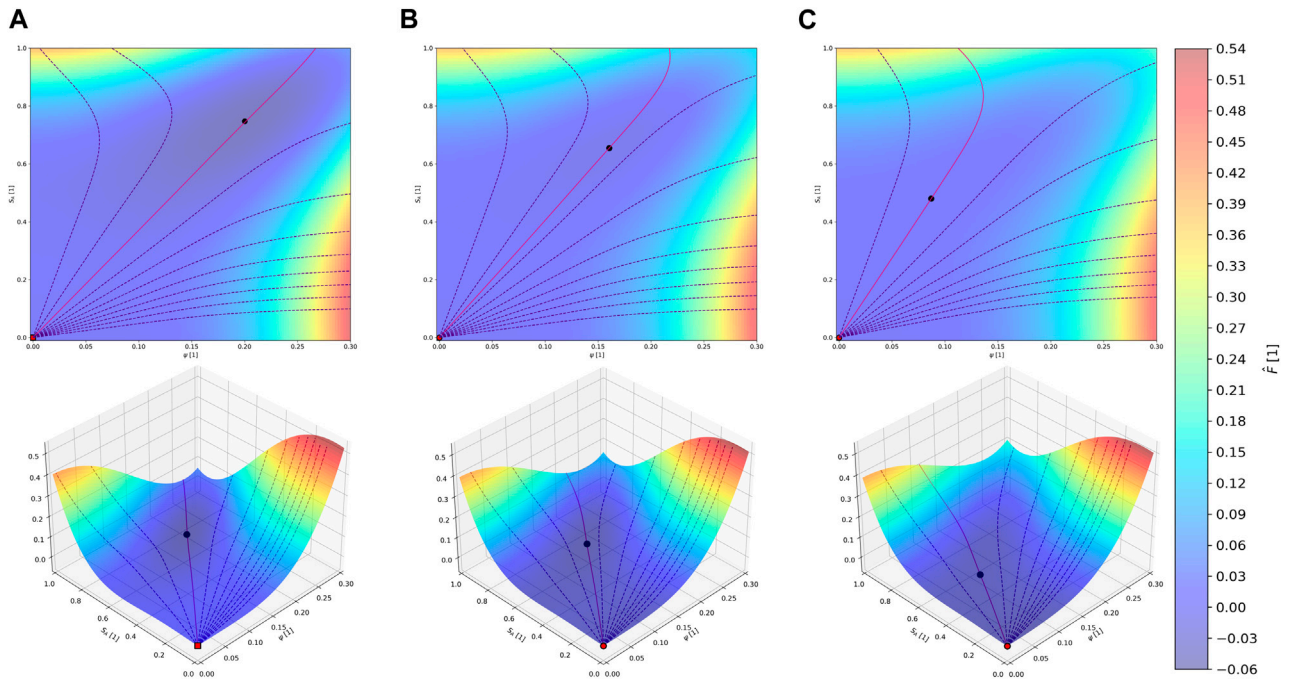

FIGURE 7
Geodesics superimposed on the (ψ, S_A)-energy landscape at the same three temperatures **(A–C)** and with the marker styles listed in Table 2. The parameters used are listed in Figure 3. The circular marker presents the SmA state at those temperatures. All lines, dashed and continuous, are geodesics; however, the continuous line connects both the isotropic and SmA primary roots.

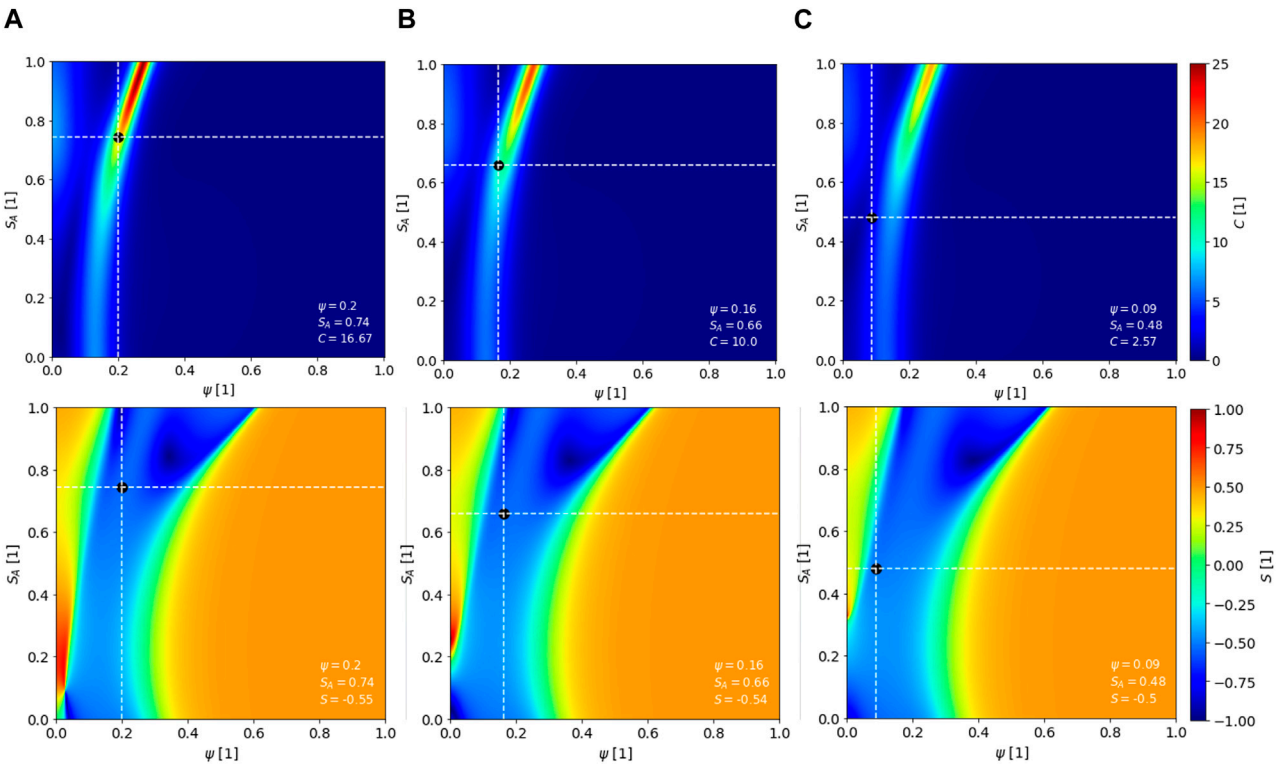

FIGURE 8
Casorati curvature ***C*** (upper set) and **s**hape ***S*** coefficient (lower set) heatmaps as a function of ψ and S_A at the same three temperatures **(A–C)** and with the marker styles listed in Table 2. The parameters used are listed in Figure 3. The coordinates on the bottom-right corner correspond to the SmA phase (black dot) with their Casorati and shape coefficient values at each temperature.

in (A), and it starts to bend in the direction of a greater change in energy as the shallow quench (C) is reached. Another important observation is that the change in shape, direction, and bending are reflected in the LOC as the quench regime changes, as opposed to what the geodesics show in this figure.

3.4 Shape coefficient and Casorati curvature

Figure 8 shows the Casorati (C) curvature (top) and shape (S) coefficient (bottom) heatmaps as a function of the OPs (ψ, S_A) coordinates. The Casorati curvature and shape coefficient were computed using Equation 2.20 and the definitions in Supplementary Appendix A2 at the temperatures listed in Table 1 for the three representative quench zones. The primary root that corresponds to the most stable phase at each temperature was included in the bottom-right corner of each plot containing the Casorati curvature and shape coefficient values at those coordinates.

The Casorati curvature presents major activity along the zone where the critical points move as the temperature varies. It can be noted that the Casorati curvature decreases as the quench depth decreases, which follows a trend toward the isotropic transition, where both order parameters are zero and the energy surface is planar and, hence, $C = 0$. The crucial feature of the computed $C = C(\psi, S_A)$ is the presence of a bent vertical tubular region of higher C values in a matrix of low C. Within this high C tube, the curvedness increases as we move toward and beyond the SmA phase in the SD and NG zones. In the shallow quench, the increase is attenuated as the energy surface evolves toward planarity. Interestingly, an approximate scaling for the high C tube is a power law $S_A \approx (\psi - 0.1)^n$; $n \approx 0.01$; more accurate fittings require parameters, but the important point is that smectic ordering produces a large increase in orientational ordering along the high C tube. Furthermore, if we compare Figure 8A (top right) with the energy landscape of Figure 5 (bottom left) in the spinodal mode, we see that the axis of the high C tube follows the steepest descent line that starts at the metastable plastic crystal and traverses the stable SmA phase to end at the higher energy states $(\psi \approx 0.3, S_A \approx 1)$. Hence, the C tube is another distinguishing feature of the energy landscape.

We now search for the distinguished feature(s) of the shape S coefficient. Figure 8 (bottom) shows that the shape coefficient associated with the local minima at each temperature does not reach $S = -1$ or a perfect ideal cup shape, as previously observed from the findings of Wang et al. (2020). The reason behind this is the energy surface anisotropy that originates from the LdG polynomial structure (Eq. 2.7), as observed already in non-circular level-set curves (see elliptical curves surrounding minima in Figure 4). In addition, we noticed that for stability, the shape coefficient follows a trend, assigning the local minima to a surface lying between a cup (-1) and a rut (-0.5) shape; for completeness, we note that the intermediate value $(S = -0.75)$ is usually denoted as a trough. This shape condition of local minima $(-1 < S < -0.5)$ corresponds to a shape with small and large principal curvatures. This behavior is also

supported by the LOC network seen in Figure 6. In more quantitative detail, Figure 8 shows that the correspondence between the OPs of the local minimum and the energy surface shape is as follows:

- Spinodal decomposition mode: $S(\psi = 0.2, S_A = 0.74) = -0.55$, and the shape is between a rut and a trough.
- Nucleation and growth mode: $S(\psi = 0.16, S_A = 0.66) = -0.54$, and the shape is between a rut and a trough.
- Shallow quench mode: $S(\psi = 0, S_A = 0) = -0.84$, and the shape is between a trough and a cup.

Figure 8 (bottom) shows another distinguishing feature of the shape index, with the blue concave-up (ridge) domain describing a bent channel that narrows and widens as the order increases. The outer red domains indicate unstable or concave-down (cap) states, and the green boundaries are saddle-like shapes. Hence, the shape landscape for smectic phases follows the previously established rules (Wang et al., 2020) of shape coexistence, where moving from left to right in each panel from Figure 8 (bottom), we find the following:

$$\underbrace{S = 0.75 \rightarrow S = 0.5}_{\text{concave down}} \rightarrow \underbrace{S = 0}_{\text{saddle}} \rightarrow$$
$$S = \underbrace{-0.5 \rightarrow S = -0.75 \rightarrow S - 0.5}_{\text{concave-up}} \rightarrow \underbrace{S = 0}_{\text{saddle}} \rightarrow \underbrace{S = 0.5 \rightarrow S = 0.75}_{\text{concave down}},$$

where saddles are needed to separate minima from maxima, which is in agreement with the polynomial theorem for critical point index $i_F = +1$ given in Table 2 and Equation 2.12.

Figure 9 takes the geodesics presented in Figure 7 and projects them on the Casorati and shape coefficient heatmaps from Figure 8 for each temperature according to the three quenching zones listed in Table 1.

The main features gleaned from the Casorati-I-SmA geodesic correlations from Figure 9 (top) are the following:

- The intersection of the geodesic with the high curvedness Casorati tube occurs at high S_A values but is eventually lost because the slope of the geodesic increases with T, while the Casorati tube bends to the right. For the intersection of the geodesic and tube, we need a geodesic slope m given by the following equation:

$$S_{A,C} \approx (\psi - 0.1)^{0.01};$$
$$S_{A,G} \approx m(T)\psi \rightarrow S_{A,C} = S_{A,G} \rightarrow (\psi - 0.1)^{0.01}$$
$$= m(T)\psi \rightarrow m(T) = \frac{(\psi - 0.1)^{0.01}}{\psi},$$

where the subscripts (C, G) denote the Casorati and geodesics. This is only possible in the deep and intermediate quenches.

- The I-SmA geodesics for NG and SD modes largely avoid the higher Casorati curvatures, indicating paths of lower curvatures.

The main features gleaned from shape coefficient-I-SmA geodesic correlations from Figure 9 (bottom) are as follows:

- The geodesic path remains well-contained in the shape index channel comprehending ruts and trough concave-up shapes, except at low OP and low-temperature values, where saddle-like (green areas close to the origin) and concave-down (red areas close to the origin) shapes arise.
- The development of SmA droplets that may form from an intermediate quench into the NG mode starts with a $S \approx -0.54$ in the smectic phase and ends with $S \approx -0.84$ in the isotropic state; therefore, the geodesic path to drop formation involves relatively modest shape configurational changes.

Figure 10 integrates the curve families on the energy landscape corresponding to the SD quench regime ($T = 330$ K), the stable SmA phase (black dot), and an unstable isotropic phase. It presents the steepest descent lines, LOC, and geodesics on the (ψ, S_A)-energy landscape. The linear diagonal geodesic connecting the isotropic (unstable)-to-smectic A (stable) phases partitions the rut and trough region and serves as an attracting manifold for maximal LOC and curves of the steepest descent; the congruence of these three lines indicates why, at this temperature, SmA is the attractor. On the bottom right high-energy area, the congruence is now between minimal LOC, curves of steepest descent, and curved geodesics, indicating a repelling landscape.

4 Conclusion

In this paper, we developed, implemented, and tested a novel computational geometrical method that complements classical liquid crystal phase transition modeling for the complex case of two-order-parameter symmetry breaking. This approach uses complementary geometric schemes to link the thermodynamic energy landscape of the isotropic-to-smectic A liquid crystal direct phase transition with novel soft-matter geometric metrics such as the Casorati curvature and shape coefficient. We summarize the results and their significance as follows:

1. A previously presented and comprehensive study of the Landau–de Gennes free-energy model (De Gennes and Prost, 1993; Pleiner et al., 2000; Larin, 2004; Oswald and Pieranski, 2005b; Donald et al., 2006; Biscari et al., 2007; Abukhdeir and Rey, 2009b; Nandi et al., 2012; Izzo and De Oliveira, 2019) for the direct isotropic-to-smectic A transition with well-known material properties (Urban et al., 2005; Abukhdeir and Rey, 2008; Coles and Strazielle, 2011) formed the basis of the theory and computational modeling characterization of phase ordering with two non-conserved order parameters.
2. The Landau free-energy landscape was obtained using explicit Monge surface parametrization as a function of orientational and positional orders, allowing the deployment of, in a simple manner, differential geometry calculations (Eq. 2.7)
3. The index polynomial theorem (Eq. 2.12) for the number of critical roots as a function of quench depth revealed the importance of saddle roots in the spinodal and nucleation and growth region; without the knowledge of parametric free-energy coefficient data, the theorem shows that the maximum number of critical roots is 3x3 since the free energy is a quartic polynomial in the two order parameters.

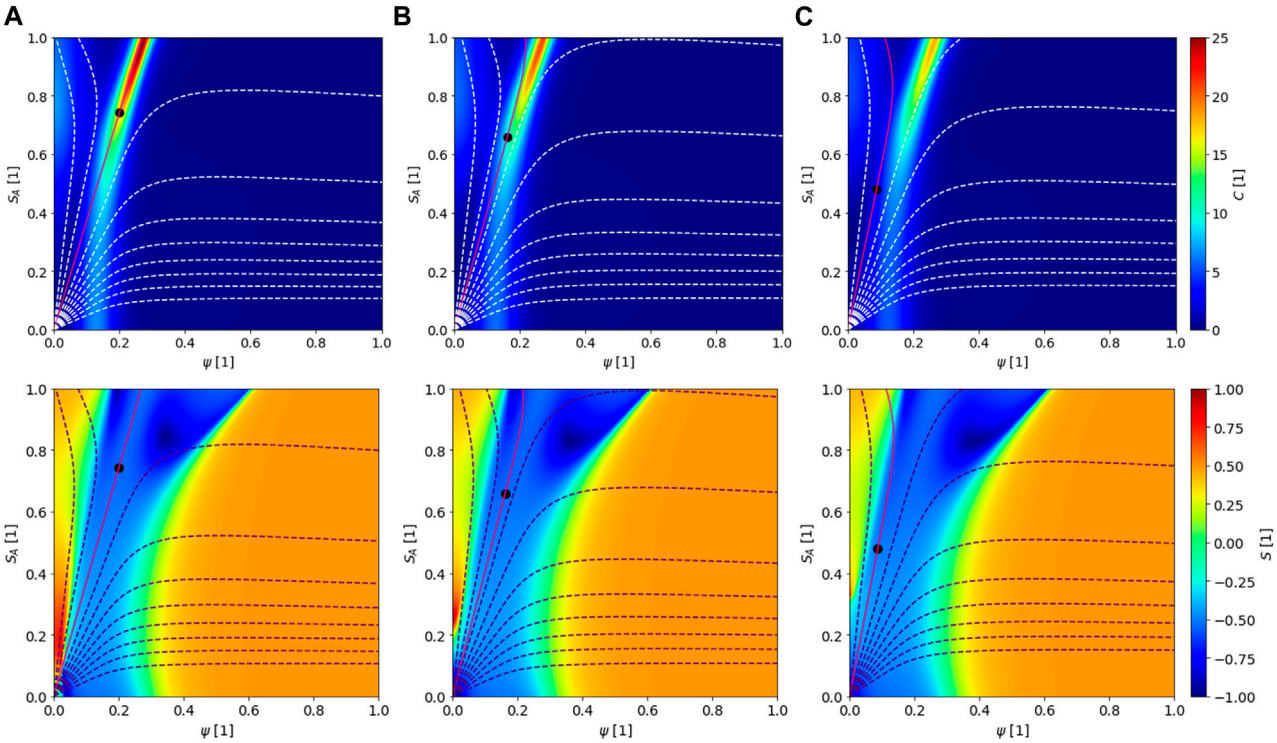

FIGURE 9
Geodesics projected on the Casorati curvature ***C*** (upper set) and shape ***S*** coefficient (lower set) heatmaps from Figure 8 as a function of ψ and S_A at the same three temperatures **(A-C)** and with the marker styles listed in Table 2. The parameters used are listed in Figure 3. The circular marker presents the SmA phase at those temperatures. The geodesics are the same from Figure 7, with different color scheme for visualization purposes. The continuous purple lines are geodesics that connect both the isotropic and SmA phases.

4. Using high-performance computing and high-fidelity numerical methods for nonlinear algebraic and differential equations, the following curve families were calculated (Sections 3.2 and 3.3): level-set-steepest descent and geodesic-principal curvatures. These special curves revealed the location of critical points already predicted by the index theorem, directions of small and large curvatures, and minimal length connections between isotropic and smectic roots. In particular, linear geodesics joining isotropic and smectic states in nucleation and growth and spinodal quenches revealed phase transformation paths. The level-set curves around stable roots were elliptical, indicating anisotropy originating from the Landau free-energy polynomial.
5. The emergence of metastable plastic crystals at deep quenches and unstable nematic states at deep and intermediate quenches was characterized, and their annihilation through supercritical and saddle-node bifurcation was captured, re-emphasizing results from the index polynomial theorem. The relevance of the nematic or plastic order at the interfaces of smectic A drops in an isotropic matrix was pointed out.
6. Previously presented measures of shape and curvedness (Casorati) in soft-matter materials were used (Section 3.4) to characterize the energy landscape with purely geometric measures instead of order parameter coordinates. The calculations were integrated with the curve families, showing consistency and revealing that the Casorati landscape is a bent, higher-curved tube embedded in a low-curvedness matrix; the tube is well-fitted with a power law function. The smectic A root resides inside this tube and moves downward as the temperature increases. The shape coefficient landscape is characterized by a wide channel of concave-up shapes separated from an area of concave-down shapes by saddle-like interfaces, which is in agreement with shape coexistence phenomena.
7. Plotting all the curve families (point 4 above) in the energy landscape, we find that at large quench, the isotropic-to-smectic A geodesic is an attractor for maximal lines of curvature and curves of the steepest descent, explaining the stability of the smectic A state.

The combination of parameter-free predictions from polynomial theorems with the computational geometry of the free-energy landscape contributes to the evolving understanding and characterization of the isotropic-to-smectic A transition, which is of high interest to biological colloidal liquid crystals, such as in the precursors to the mussel byssus (Renner-Rao et al., 2019; Harrington and Fratzl, 2021; Jehle et al., 2021) through droplet nucleation/growth and colloidal impingement. We demonstrated that the presence of two non-conserved order parameters creates challenges in equilibrium spatially homogeneous simulations, but how time-dependent processes such as droplet growth resolve the couplings of shape–size–structure–interface remains to be elucidated in future work by building on the present results and methods.

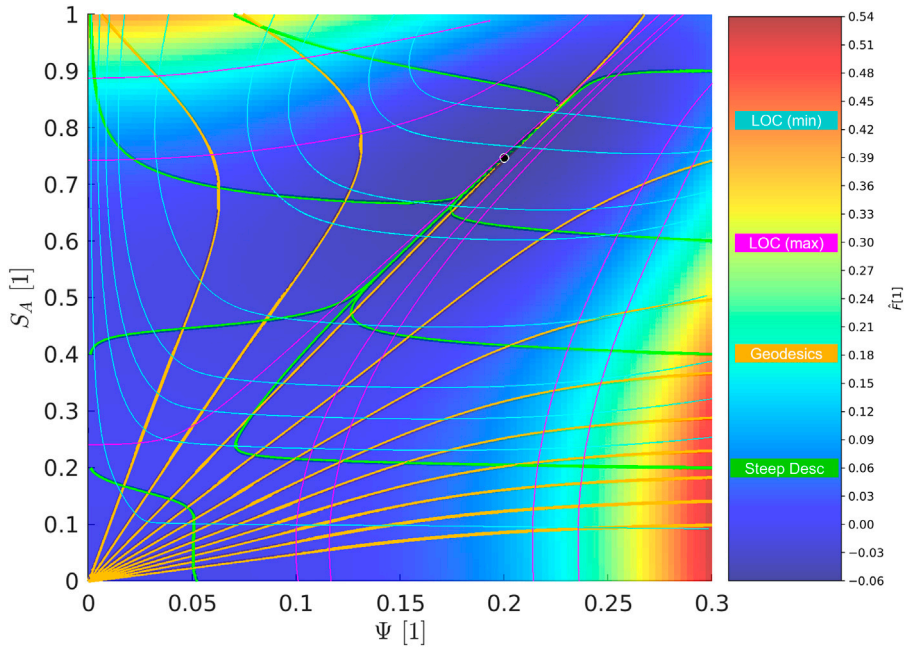

FIGURE 10
(ψ, S_A)-energy landscape for temperature (A) as listed in Table 2, integrating the steepest descent lines (green), LOC (cyan-min and magenta-max), and geodesics (orange) curves. The black dot represents the stable primary root, SmA phase.

Data availability statement

Data related to this work will be made available by request to the authors. Requests to access the datasets should be directed to ADR, alejandro.rey@mcgill.ca.

Author contributions

DZ: writing–original draft, conceptualization, data curation, formal analysis, investigation, methodology, software, validation, visualization, and writing–review and editing. ZW: conceptualization, writing–review and editing, validation, and methodology. ND: conceptualization, supervision, and writing–review and editing. MH: conceptualization, supervision, and writing–review and editing. AR: conceptualization, validation, writing–review and editing, formal analysis, funding acquisition, project administration, resources, and supervision.

Funding

The author(s) declare that financial support was received for the research, authorship, and/or publication of this article. This work was supported by the Fonds de Recherche du Québec (FRQNT) (2021-PR-284991) and the Natural Science and Engineering Research Council of Canada (NSERC) (#223086). Author DUZC thanks Consejo Nacional de Humanidades, Ciencia y Tecnología (CONAHCYT) (853563), and McGill Engineering Doctoral Award (MEDA) scholarships for financial support.

Acknowledgments

The authors acknowledge Digital Research Alliance of Canada (ID 4700) for computational resources and technical support.

Conflict of interest

The authors declare that the research was conducted in the absence of any commercial or financial relationships that could be construed as a potential conflict of interest.

Publisher's note

Supplementary material

The Supplementary Material for this article can be found online at: https://www.frontiersin.org/articles/10.3389/frsfm.2024.1359128/full#supplementary-material

References

Abbena, E., Salamon, S., and Gray, A. (2017). *Modern differential geometry of curves and surfaces with Mathematica*. China: CRC Press.

Abukhdeir, N. M. (2009). Growth, dynamics, and texture modeling of the lamellar smectic-A liquid crystalline transition. *Doctor of Philosophy*. Canada: McGill University.

Abukhdeir, N. M., and Rey, A. D. (2008). Simulation of spherulite growth using a comprehensive approach to modeling the first-order isotropic/smectic-A mesophase transition. *arXiv Prepr. arXiv:0807.4525*. doi:10.48550/arXiv.0807.4525

Abukhdeir, N. M., and Rey, A. D. (2009a). Metastable nematic preordering in smectic liquid crystalline phase transitions. *Macromolecules* 42, 3841–3844. doi:10.1021/ma900796b

Abukhdeir, N. M., and Rey, A. D. (2009b). Nonisothermal model for the direct isotropic/smectic-A liquid-crystalline transition. *Langmuir* 25, 11923–11929. doi:10.1021/la9015965

Abukhdeir, N. M., and Rey, A. D. (2009c). Shape-dynamic growth, structure, and elasticity of homogeneously oriented spherulites in an isotropic/smectic-A mesophase transition. *Liq. Cryst.* 36, 1125–1137. doi:10.1080/02678290902878754

Aguilar Gutierrez, O. F., and Rey, A. D. (2018). Extracting shape from curvature evolution in moving surfaces. *Soft Matter* 14, 1465–1473. doi:10.1039/c7sm02409f

Bellini, T., Clark, N. A., and Link, D. R. (2002). Isotropic to smectic a phase transitions in a porous matrix: a case of multiporous phase coexistence. *J. Phys. Condens. Matter* 15, S175–S182. doi:10.1088/0953-8984/15/1/322

Berent, K., Cartwright, J. H. E., Checa, A. G., Pimentel, C., Ramos-Silva, P., and Sainz-Díaz, C. I. (2022). Helical microstructures in molluscan biomineralization are a biological example of close packed helices that may form from a colloidal liquid crystal precursor in a twist--bend nematic phase. *Phys. Rev. Mater.* 6, 105601. doi:10.1103/physrevmaterials.6.105601

Biscari, P., Calderer, M. C., and Terentjev, E. M. (2007). Landau-de Gennes theory of isotropic-nematic-smectic liquid crystal transitions. *Phys. Rev. E Stat. Nonlin Soft Matter Phys.* 75, 051707. doi:10.1103/physreve.75.051707

Blinov, L. M. (2011). *Structure and properties of liquid crystals*. Dordrecht: Springer.

Bowick, M. J., Kinderlehrer, D., Menon, G., and Radin, C. (2017). Mathematics and materials, *American mathematical soc*.

Bradley, P. A. (2019). On the physicochemical control of collagen fibrilligenesis and biomineralization. *Doctor of Philosophy*. USA: Northeastern University.

Bukharina, D., Kim, M., Han, M. J., and Tsukruk, V. V. (2022). Cellulose nanocrystals' assembly under ionic strength variation: from high orientation ordering to a random orientation. *Langmuir* 38, 6363–6375. doi:10.1021/acs.langmuir.2c00293

Bunsell, A. R., Joannès, S., and Thionnet, A. (2021). *Fundamentals of fibre reinforced composite materials*. Germany: CRC Press.

Cai, A., Abdali, Z., Saldanha, D. J., Aminzare, M., and Dorval Courchesne, N.-M. (2023). Endowing textiles with self-repairing ability through the fabrication of composites with a bacterial biofilm. *Sci. Rep.* 13, 11389. doi:10.1038/s41598-023-38501-2

Chahine, G., Kityk, A. V., Démarest, N., Jean, F., Knorr, K., Huber, P., et al. (2010). Collective molecular reorientation of a calamitic liquid crystal (12CB) confined in alumina nanochannels. *Phys. Rev. E* 82, 011706. doi:10.1103/physreve.82.011706

Coles, H. J., and Strazielle, C. (2011). The order-disorder phase transition in liquid crystals as a function of molecular structure. I. The alkyl cyanobiphenyls. *Mol. Cryst. Liq. Cryst.* 55, 237–250. doi:10.1080/00268947908069805

Collings, P. J. (1997). *Phase structures and transitions in thermotropic liquid crystals handbook of liquid crystal research*.

Collings, P. J., and Goodby, J. W. (2019). *Introduction to liquid crystals: chemistry and physics*. Germany: Crc Press.

Collings, P. J., and Hird, M. (2017). *Introduction to liquid crystals chemistry and physics*. Germany: CRC Press.

Copic, M., and Mertelj, A. (2020). Q-tensor model of twist-bend and splay nematic phases. *Phys. Rev. E* 101, 022704. doi:10.1103/physreve.101.022704

Das, A. K., and Mukherjee, P. K. (2009). Phenomenological theory of the direct isotropic to hexatic-B phase transition. *J. Chem. Phys.* 130, 054901. doi:10.1063/1.3067425

de Gennes, P. G. (2007). Some remarks on the polymorphism of smectics. *Mol. Cryst. Liq. Cryst.* 21, 49–76. doi:10.1080/15421407308083313

de Gennes, P.-G., and Prost, J. (1993). *The physics of liquid crystals*. Oxford: Oxford University Press.

de Luca, G., and Rey, A. D. (2004). Chiral front propagation in liquid-crystalline materials: formation of the planar monodomain twisted plywood architecture of biological fibrous composites. *Phys. Rev. E* 69, 011706. doi:10.1103/physreve.69.011706

de Luca, G., and Rey, A. D. (2006). Dynamic interactions between nematic point defects in the spinning extrusion duct of spiders. *J. Chem. Phys.* 124, 144904. doi:10.1063/1.2186640

de Luca, G., and Rey, A. (2003). Monodomain and polydomain helicoids in chiral liquid-crystalline phases and their biological analogues. *Eur. Phys. J. E* 12, 291–302. doi:10.1140/epje/i2002-10164-3

Demirci, N., and Holland, M. A. (2022). Cortical thickness systematically varies with curvature and depth in healthy human brains. *Hum. Brain Mapp.* 43, 2064–2084. doi:10.1002/hbm.25776

Demus, D., Goodby, J. W., Gray, G. W., Spiess, H. W., and Vill, V. (2008a). *Handbook of liquid crystals*.

Demus, D., Goodby, J. W., Gray, G. W., Spiess, H. W., and Vill, V. (2008b). *Handbook of liquid crystals, volume 3: high molecular weight liquid crystals*. USA: John Wiley and Sons.

Demus, D., Goodby, J. W., Gray, G. W., Spiess, H. W., and Vill, V. (2011). *Handbook of liquid crystals, volume 2A: low molecular weight liquid crystals I: calamitic liquid crystals*. USA: John Wiley and Sons.

Deng, F., Dang, Y., Tang, L., Hu, T., Ding, C., Hu, X., et al. (2021). Tendon-inspired fibers from liquid crystalline collagen as the pre-oriented bioink. *Int. J. Biol. Macromol.* 185, 739–749. doi:10.1016/j.ijbiomac.2021.06.173

Dierking, I., and al-Zangana, S. (2017). Lyotropic liquid crystal phases from anisotropic nanomaterials. *Nanomater. (Basel)* 7, 305. doi:10.3390/nano7100305

Dilisi, G. A. (2019). in *An introduction to liquid crystals*. Editor J. J. DELUCA (New York: Morgan and Claypool Publishers).

Do Carmo, M. P. (2016). *Differential geometry of curves and surfaces: revised and updated*. second edition. New York: Courier Dover Publications.

Dogic, Z., and Fraden, S. (2001). Development of model colloidal liquid crystals and the kinetics of the isotropic-smectic transition. *Philosophical Trans. R. Soc. a-Mathematical Phys. Eng. Sci.* 359, 997–1015. DOI, M. 1981. doi:10.1098/rsta.2000.0814

Doi, M. 2022 Molecular dynamics and rheological properties of concentrated solutions of rodlike polymers in isotropic and liquid crystalline phases. *J. Polym. Sci. Polym. Phys. Ed.* 19, 229–243. doi:10.1002/pol.1981.180190205

Donald, A. M., Windle, A. H., and Hanna, S. (2006). *Liquid crystalline polymers*. Cambridge: Cambridge University Press.

Durfee, A., Kronenfeld, N., Munson, H., Roy, J., and Westby, I. (1993). Counting critical points of real polynomials in two variables. *Am. Math. Mon.* 100, 255–271. doi:10.2307/2324459

Farouki, R. T. (1998). On integrating lines of curvature. *Comput. Aided Geom. Des.* 15, 187–192. doi:10.1016/s0167-8396(97)00022-8

Fischer, S., and Karplus, M. (1992). Conjugate peak refinement: an algorithm for finding reaction paths and accurate transition states in systems with many degrees of freedom. *Chem. Phys. Lett.* 194, 252–261. doi:10.1016/0009-2614(92)85543-j

Garti, N., Somasundaran, P., and Mezzenga, R. (2012). *Self-assembled supramolecular architectures: lyotropic liquid crystals*. USA: John Wiley and Sons.

Golmohammadi, M., and Rey, A. D. (2009). Thermodynamic modelling of carbonaceous mesophase mixtures. *Liq. Cryst.* 36, 75–92. doi:10.1080/02678290802666218

Golmohammadi, M., and Rey, A. D. (2010). Structural modeling of carbonaceous mesophase amphotropic mixtures under uniaxial extensional flow. *J. Chem. Phys.* 133, 034903. doi:10.1063/1.3455505

Gorkunov, M., Osipov, M., Lagerwall, J., and Giesselmann, F. (2007). Order-disorder molecular model of the smectic-A–smectic-C phase transition in materials with conventional and anomalously weak layer contraction. *Phys. Rev. E* 76, 051706. doi:10.1103/physreve.76.051706

Gudimalla, A., Thomas, S., and Zidanšek, A. (2021). Phase behaviour of n-CB liquid crystals confined to controlled pore glasses. *J. Mol. Struct.* 1235, 130217. doi:10.1016/j.molstruc.2021.130217

Gurevich, S., Soule, E., Rey, A., Reven, L., and Provatas, N. (2014). Self-assembly via branching morphologies in nematic liquid-crystal nanocomposites. *Phys. Rev. E* 90, 020501. doi:10.1103/physreve.90.020501

Gurin, P., Odriozola, G., and Varga, S. (2021). Enhanced two-dimensional nematic order in slit-like pores. *New J. Phys.* 23, 063053. doi:10.1088/1367-2630/ac05e1

Han, J. Q., Luo, Y., Wang, W., Zhang, P. W., and Zhang, Z. F. (2015). From microscopic theory to macroscopic theory: a systematic study on modeling for liquid crystals. *Archive Ration. Mech. Analysis* 215, 741–809. doi:10.1007/s00205-014-0792-3

Han, W., and Rey, A. (1993). Supercritical bifurcations in simple shear flow of a non-aligning nematic: reactive parameter and director anchoring effects. *J. Newt. fluid Mech.* 48, 181–210. doi:10.1016/0377-0257(93)80070-r

Harrington, M. J., and Fratzl, P. (2021). Natural load-bearing protein materials. *Prog. Mater. Sci.* 120, 100767. doi:10.1016/j.pmatsci.2020.100767

Hawkins, R. J., and April, E. W. (1983). "Liquid crystals in living tissues," in *Advances in liquid crystals*. Editor G. H. BROWN (Germany: Elsevier).

Hormann, K., and Zimmer, J. (2007). On Landau theory and symmetric energy landscapes for phase transitions. *J. Mech. Phys. Solids* 55, 1385–1409. doi:10.1016/j.jmps.2007.01.004

Idziak, S. H. J., Koltover, I., Davidson, P., Ruths, M., Li, Y., Israelachvili, J. N., et al. (1996). Structure under confinement in a smectic-A and lyotropic surfactant hexagonal phase. *Phys. B Condens. Matter* 221, 289–295. doi:10.1016/0921-4526(95)00939-6

Izzo, D., and de Oliveira, M. J. (2019). Landau theory for isotropic, nematic, smectic-A, and smectic-C phases. *Liq. Cryst.* 47, 99–105. doi:10.1080/02678292.2019.1631968

Jackson, K., Peivandi, A., Fogal, M., Tian, L., and Hosseinidoust, Z. (2021). Filamentous phages as building blocks for bioactive hydrogels. *ACS Appl. Bio Mater.* 4, 2262–2273. doi:10.1021/acsabm.0c01557

Jákli, A., and Saupe, A. (2006). *One-and two-dimensional fluids: properties of smectic, lamellar and columnar liquid crystals*. New York: CRC Press.

Jehle, F., Priemel, T., Strauss, M., Fratzl, P., Bertinetti, L., and Harrington, M. J. (2021). Collagen pentablock copolymers form smectic liquid crystals as precursors for mussel byssus fabrication. *ACS Nano* 15, 6829–6838. doi:10.1021/acsnano.0c10457

Khadem, S. A., and Rey, A. D. (2021). Nucleation and growth of cholesteric collagen tactoids: a time-series statistical analysis based on integration of direct numerical simulation (DNS) and long short-term memory recurrent neural network (LSTM-RNN). *J. Colloid Interface Sci.* 582, 859–873. doi:10.1016/j.jcis.2020.08.052

Khan, B. C., and Mukherjee, P. K. (2021). Isotropic to smectic-A phase transition in taper-shaped liquid crystal. *J. Mol. Liq.* 329, 115539. doi:10.1016/j.molliq.2021.115539

Knight, D., and Vollrath, F. (1999). Hexagonal columnar liquid crystal in the cells secreting spider silk. *Tissue Cell.* 31, 617–620. doi:10.1054/tice.1999.0076

Knill, O. (2012). A graph theoretical Poincaré-Hopf theorem. *arXiv Prepr. arXiv: 1201.1162*. doi:10.48550/arXiv.1201.1162

Koenderink, J. J., and van Doorn, A. J. (1992). Surface shape and curvature scales. *Image Vis. Comput.* 10, 557–564. doi:10.1016/0262-8856(92)90076-f

Kyrylyuk, A. V., Anne van de Haar, M., Rossi, L., Wouterse, A., and Philipse, A. P. (2011). Isochoric ideality in jammed random packings of non-spherical granular matter. *Soft Matter* 7, 1671–1674. doi:10.1039/c0sm00754d

Lagerwall, J. P. (2016). An introduction to the physics of liquid crystals. *Fluids, Colloids Soft Mater. Introd. Soft Matter Phys.*, 307–340. doi:10.1002/9781119220510.ch16

Larin, E. S. (2004). Phase diagram of transitions from an isotropic phase to nematic and smectic (uniaxial, biaxial) phases in liquid crystals with achiral molecules. *Phys. Solid State* 46, 1560–1568. doi:10.1134/1.1788795

Lenoble, J., Campidelli, S., Maringa, N., Donnio, B., Guillon, D., Yevlampieva, N., et al. (2007). Liquid– crystalline Janus-type fullerodendrimers displaying tunable smectic– columnar mesomorphism. *J. Am. Chem. Soc.* 129, 9941–9952. doi:10.1021/ja071012o

Li, C.-Z., Matsuo, Y., and Nakamura, E. (2009). Luminescent bow-tie-shaped decaaryl[60]fullerene mesogens. *J. Am. Chem. Soc.* 131, 17058–17059. doi:10.1021/ja907908m

Liu, B., Besseling, T. H., Hermes, M., Demirörs, A. F., Imhof, A., and van Blaaderen, A. (2014). Switching plastic crystals of colloidal rods with electric fields. *Nat. Commun.* 5, 3092. doi:10.1038/ncomms4092

Liu, X., Chen, H., and Ortner, C. (2022). Stability of the minimum energy path. *arXiv Prepr. arXiv:2204.00984*. doi:10.1007/s00211-023-01391-7

Maekawa, T. (1996). *Computation of shortest paths on free-form parametric surfaces*.

Manolakis, I., and Azhar, U. (2020). Recent advances in mussel-inspired synthetic polymers as marine antifouling coatings. *Coatings* 10, 653. doi:10.3390/coatings10070653

Massi, F., and Straub, J. E. (2001). Energy landscape theory for Alzheimer's amyloid β-peptide fibril elongation. *Proteins Struct. Funct. Bioinforma.* 42, 217–229. doi:10.1002/1097-0134(20010201)42:2<217::aid-prot90>3.0.co;2-n

Matthews, J. A., Wnek, G. E., Simpson, D. G., and Bowlin, G. L. (2002). Electrospinning of collagen nanofibers. *Biomacromolecules* 3, 232–238. doi:10.1021/bm015533u

Milette, J., Toader, V., Soulé, E. R., Lennox, R. B., Rey, A. D., and Reven, L. (2013). A molecular and thermodynamic view of the assembly of gold nanoparticles in nematic liquid crystal. *Langmuir* 29, 1258–1263. doi:10.1021/la304189n

Miller, W. L. (1925). The method of willard gibbs in chemical thermodynamics. *Chem. Rev.* 1, 293–344. doi:10.1021/cr60004a001

Mohieddin Abukhdeir, N., and Rey, A. D. (2008a). Defect kinetics and dynamics of pattern coarsening in a two-dimensional smectic-A system. *New J. Phys.* 10, 063025. doi:10.1088/1367-2630/10/6/063025

Mohieddin Abukhdeir, N., and Rey, A. D. 2008b. Modeling the isotropic/smectic-C tilted lamellar liquid crystalline transition.

Mukherjee, P. K. (2014). Isotropic to smectic-A phase transition: a review. *J. Mol. Liq.* 190, 99–111. doi:10.1016/j.molliq.2013.11.001

Mukherjee, P. K. (2021). Advances of isotropic to smectic phase transitions. *J. Mol. Liq.* 340, 117227. doi:10.1016/j.molliq.2021.117227

Mukherjee, P. K., Pleiner, H., and Brand, H. R. (2001). Simple Landau model of the smectic-A-isotropic phase transition. *Eur. Phys. J. E* 4, 293–297. doi:10.1007/s101890170111

Nandi, B., Saha, M., and Mukherjee, P. K. (2012). Landau theory of the direct smectic-A to isotropic phase transition. *Int. J. Mod. Phys. B* 11, 2425–2432. doi:10.1142/s0217979297001234

Nesrullajev, A. (2022). Optical refracting properties, birefringence and order parameter in mixtures of liquid crystals: direct smectic A – Isotropic and reverse isotropic – smectic A phase transitions. *J. Mol. Liq.* 345, 117716. doi:10.1016/j.molliq.2021.117716

Oh, C. S. (1977). Induced smectic mesomorphism by incompatible nematogens. *Mol. Cryst. Liq. Cryst.* 42, 1–14. doi:10.1080/15421407708084491

Oswald, P., and Pieranski, P. (2005a). *Nematic and cholesteric liquid crystals: concepts and physical properties illustrated by experiments*. China: CRC Press.

Oswald, P., and Pieranski, P. (2005b). *Smectic and columnar liquid crystals*.

Paget, J., Alberti, U., Mazza, M. G., Archer, A. J., and Shendruk, T. N. (2022). Smectic layering: Landau theory for a complex-tensor order parameter. *J. Phys. A Math. Theor.* 55, 354001. doi:10.1088/1751-8121/ac80df

Palffy-Muhoray, P. (1999). Dynamics of filaments during the isotropic-smectic A phase transition. *J. Nonlinear Sci.* 9, 417–437. doi:10.1007/s003329900075

Petrov, A. G. (2013). Flexoelectricity in lyotropics and in living liquid crystals. *Flexoelectricity Liq. Cryst. theory, Exp. Appl. World Sci.* doi:10.1142/9781848168008_0007

Pevnyi, M. Y., Selinger, J. V., and Sluckin, T. J. (2014). Modeling smectic layers in confined geometries: order parameter and defects. *Phys. Rev. E Stat. Nonlin Soft Matter Phys.* 90, 032507. doi:10.1103/physreve.90.032507

Picken, S. J. (1990). Orientational order in aramid solutions determined by diamagnetic susceptibility and birefringence measurements. *Macromolecules* 23, 464–470. doi:10.1021/ma00204a019

Pikin, S. A. (1991). *Structural transformations in liquid crystals*.

Pleiner, H., Mukherjee, P. K., and Brand, H. R. (2000). Direct transitions from isotropic to smectic phases. *Proc. Freiburger Arbeitstagung Flussigkristalle*, P59.

Popa-Nita, V. (1999). Statics and kinetics at the nematic-isotropic interface in porous media. *Eur. Phys. J. B-Condensed Matter Complex Syst.* 12, 83–90. doi:10.1007/s100510050981

Popa-Nita, V., and Sluckin, T. J. (2007). *Waves at the nematic-isotropic interface: nematic-non-nematic and polymer-nematic mixtures*. Netherlands: Springer, 253–267.

Pouget, E., Grelet, E., and Lettinga, M. P. (2011). Dynamics in the smectic phase of stiff viral rods. *Phys. Rev. E Stat. Nonlin Soft Matter Phys.* 84, 041704. doi:10.1103/physreve.84.041704

Quevedo, H., Quevedo, M. N., and Sánchez, A. (2022). Geometrothermodynamics of van der Waals systems. *J. Geometry Phys.* 176, 104495. doi:10.1016/j.geomphys.2022.104495

Quevedo, H., Sánchez, A., Taj, S., and Vázquez, A. (2011). Phase transitions in geometrothermodynamics. *General Relativ. Gravit.* 43, 1153–1165. doi:10.1007/s10714-010-0996-2

Quevedo, H., Sánchez, A., and Vázquez, A. (2008). Invariant geometry of the ideal gas. *arXiv Prepr. arXiv:0811.0222*.

Renner-Rao, M., Clark, M., and Harrington, M. J. (2019). Fiber Formation from liquid crystalline collagen vesicles isolated from mussels. *Langmuir* 35, 15992–16001. doi:10.1021/acs.langmuir.9b01932

Rey, A. D. (1995). Bifurcational analysis of the isotropic-discotic nematic phase transition in the presence of extensional flow. *Liq. Cryst.* 19, 325–331. doi:10.1080/02678299508031988

Rey, A. D. (2000). Viscoelastic theory for nematic interfaces. *Phys. Rev. E* 61, 1540–1549. doi:10.1103/physreve.61.1540

Rey, A. D. (2004a). Interfacial thermodynamics of polymeric mesophases. *Macromol. theory simulations* 13, 686–696. doi:10.1002/mats.200400030

Rey, A. D. (2004b). Thermodynamics of soft anisotropic interfaces. *J. Chem. Phys.* 120, 2010–2019. doi:10.1063/1.1635357

Rey, A. D. (2006). Mechanical model for anisotropic curved interfaces with applications to surfactant-laden Liquid– liquid crystal interfaces. *Langmuir* 22, 219–228. doi:10.1021/la051974d

Rey, A. D. (2010). Liquid crystal models of biological materials and processes. *Soft Matter* 6, 3402–3429. doi:10.1039/b921576j

Rey, A. D., and Denn, M. M. (2002). Dynamical phenomena in liquid-crystalline materials. *Annu. Rev. Fluid Mech.* 34, 233–266. doi:10.1146/annurev.fluid.34.082401.191847

Rey, A. D., and Herrera-Valencia, E. E. (2012). Liquid crystal models of biological materials and silk spinning. *Biopolymers* 97, 374–396. doi:10.1002/bip.21723

Rey, A. D., Herrera-Valencia, E. E., and Murugesan, Y. K. (2013). Structure and dynamics of biological liquid crystals. *Liq. Cryst.* 41, 430–451. doi:10.1080/02678292.2013.845698

Salamonczyk, M., Zhang, J., Portale, G., Zhu, C., Kentzinger, E., Gleeson, J. T., et al. (2016). Smectic phase in suspensions of gapped DNA duplexes. *Nat. Commun.* 7, 13358. doi:10.1038/ncomms13358

Sato, C., Takeda, T., Dekura, S., Suzuki, Y., Kawamata, J., and Akutagawa, T. (2023). Chiral plastic crystal of solid-state dual rotators. *Cryst. Growth and Des.* 23, 5889–5898. doi:10.1021/acs.cgd.3c00495

Saunders, K., Hernandez, D., Pearson, S., and Toner, J. (2007). Disordering to order: de Vries behavior from a Landau theory for smectic phases. *Phys. Rev. Lett.* 98, 197801. doi:10.1103/physrevlett.98.197801

Schimming, C. D., Viñals, J., and Walker, S. W. (2021). Numerical method for the equilibrium configurations of a Maier-Saupe bulk potential in a Q-tensor model of an anisotropic nematic liquid crystal. *J. Comput. Phys.* 441, 110441. doi:10.1016/j.jcp.2021.110441

Selinger, J. V. (2016). *Introduction to the theory of soft matter: from ideal gases to liquid crystals*. Germany: Springer.

Sonnet, A. M., and Virga, E. G. (2012). *Dissipative ordered fluids: theories for liquid crystals*. Germany: Springer Science and Business Media.

Soulé, E. R., Lavigne, C., Reven, L., and Rey, A. D. (2012a). Multiple interfaces in diffusional phase transitions in binary mesogen-nonmesogen mixtures undergoing metastable phase separations. *Phys. Rev. E* 86, 011605. doi:10.1103/physreve.86.011605

Soulé, E. R., Milette, J., Reven, L., and Rey, A. D. (2012b). Phase equilibrium and structure formation in gold nanoparticles—nematic liquid crystal composites: experiments and theory. *Soft Matter* 8, 2860–2866. doi:10.1039/c2sm07091j

Soulé, E. R., Reven, L., and Rey, A. D. (2012c). Thermodynamic modelling of phase equilibrium in nanoparticles–nematic liquid crystals composites. *Mol. Cryst. Liq. Cryst.* 553, 118–126. doi:10.1080/15421406.2011.609447

Soule, E. R., and Rey, A. D. (2011). A good and computationally efficient polynomial approximation to the Maier–Saupe nematic free energy. *Liq. Cryst.* 38, 201–205. doi:10.1080/02678292.2010.539303

Soule, E. R., and Rey, A. D. (2012). Modelling complex liquid crystal mixtures: from polymer dispersed mesophase to nematic nanocolloids. *Mol. Simul.* 38, 735–750. doi:10.1080/08927022.2012.669478

Stewart, I. W. (2019). *The static and dynamic continuum theory of liquid crystals: a mathematical introduction*. Germany: Crc Press.

Tortora, M., and Jost, D. (2021). Morphogenesis and self-organization of persistent filaments confined within flexible biopolymeric shells. *arXiv Prepr.* doi:10.48550/arXiv.2107.02598

Tuckerman, L. S., and Bechhoefer, J. (1992). Dynamical mechanism for the formation of metastable phases: the case of two nonconserved order parameters. *Phys. Rev. A* 46, 3178–3192. doi:10.1103/physreva.46.3178

Turek, D. E., Simon, G. P., and Tiu, C. (2020). "Relationships among rheology, morphology, and solid-state properties in thermotropic liquid-crystalline polymers," in *Handbook of applied polymer processing technology* (Germany: CRC Press).

Urban, S., Przedmojski, J., and Czub, J. (2005). X-ray studies of the layer thickness in smectic phases. *Liq. Cryst.* 32, 619–624. doi:10.1080/02678290500116920

Viney, C. (2004). Self-assembly as a route to fibrous materials: concepts, opportunities and challenges. *Curr. Opin. Solid State and Mater. Sci.* 8, 95–101. doi:10.1016/j.cossms.2004.04.001

Vitral, E., Leo, P. H., and Vinals, J. (2019). Role of Gaussian curvature on local equilibrium and dynamics of smectic-isotropic interfaces. *Phys. Rev. E* 100, 032805. doi:10.1103/physreve.100.032805

Vitral, E., Leo, P. H., and Vinals, J. (2020). Model of the dynamics of an interface between a smectic phase and an isotropic phase of different density. *Phys. Rev. Fluids* 5, 073302. doi:10.1103/physrevfluids.5.073302

Waite, J. H., and Harrington, M. J. (2022). Following the thread: Mytilus mussel byssus as an inspired multi-functional biomaterial. *Can. J. Chem.* 100, 197–211. doi:10.1139/cjc-2021-0191

Wales, D. J. (2018). Exploring energy landscapes. *Annu. Rev. Phys. Chem.* 69, 401–425. doi:10.1146/annurev-physchem-050317-021219

Wang, H. Y., Wang, Y. Z., Tsakalakos, T., Semenovskaya, S., and Khachaturyan, A. G. (1996). Indirect nucleation in phase transformations with symmetry reduction. *Philosophical Mag. a-Physics Condens. Matter Struct. Defects Mech. Prop.* 74, 1407–1420. doi:10.1080/01418619608240732

Wang, Z., Servio, P., and Rey, A. D. (2020). Rate of entropy production in evolving interfaces and membranes under astigmatic kinematics: shape evolution in geometric-dissipation landscapes. *Entropy* 22, 909. doi:10.3390/e22090909

Wang, Z., Servio, P., and Rey, A. D. (2022a). Complex nanowrinkling in chiral liquid crystal surfaces: from shaping mechanisms to geometric statistics. *Nanomaterials* 12, 1555. doi:10.3390/nano12091555

Wang, Z., Servio, P., and Rey, A. D. (2023a). Geometry-structure models for liquid crystal interfaces, drops and membranes: wrinkling, shape selection and dissipative shape evolution. *Soft Matter* 19, 9344–9364. doi:10.1039/d3sm01164j

Wang, Z., Servio, P., and Rey, A. D. (2023b). Pattern formation, structure and functionalities of wrinkled liquid crystal surfaces: a soft matter biomimicry platform. *Front. Soft Matter* 3, 1123324. doi:10.3389/frsfm.2023.1123324

Wang, Z., Servio, P., and Rey, A. (2022b). Wrinkling pattern formation with periodic nematic orientation: from egg cartons to corrugated surfaces. *Phys. Rev. E* 105, 034702. doi:10.1103/physreve.105.034702

Ward, I. (1993). *New developments in the production of high modulus and high strength flexible polymers. Orientational Phenomena in Polymers*. Germany: Springer, 103–110.

Wojcik, M., Lewandowski, W., Matraszek, J., Mieczkowski, J., Borysiuk, J., Pociecha, D., et al. (2009). Liquid-crystalline phases made of gold nanoparticles. *Angew. Chem. Int. Ed.* 48, 5167–5169. doi:10.1002/anie.200901206

Zaluzhnyy, I. A., Kurta, R., Sprung, M., Vartanyants, I. A., and Ostrovskii, B. I. (2022). Angular structure factor of the hexatic-B liquid crystals: bridging theory and experiment. *Soft Matter* 18, 783–792. doi:10.1039/d1sm01446c

Zannoni, C. (2022). *Liquid crystals and their computer simulations*. Germany: Cambridge University Press.

Zhang, Z., Yang, X., Zhao, Y., Ye, F., and Shang, L. (2023). Liquid crystal materials for biomedical applications. *Adv. Mater.* 35, 2300220. doi:10.1002/adma.202300220

Ziabicki, A. (1993). *Orientation mechanisms in the development of high-performance fibers Orientational Phenomena in Polymers*. Germany: Springer, 1–7.